



OPEN ACCESS

EDITED BY

Karen Bemis,
Rutgers, The State University of New
Jersey, United States

REVIEWED BY

Chelsea M. Allison,
Baylor University, United States
Christoph Helo,
Johannes Gutenberg University Mainz,
Germany

*CORRESPONDENCE

Iona M. McIntosh,
✉ i.m.mcintosh@jamstec.go.jp

SPECIALTY SECTION

This article was submitted to
Volcanology,
a section of the journal
Frontiers in Earth Science

RECEIVED 07 June 2022

ACCEPTED 25 November 2022

PUBLISHED 13 December 2022

CITATION

McIntosh IM, Aoki K, Yanagishima T,
Kobayashi M, Murata M and Suzuki T
(2022), Reconstruction of submarine
eruption processes from FTIR volatile
analysis of marine tephra: Example of
Oomurodasho volcano, Japan.
Front. Earth Sci. 10:963392.
doi: 10.3389/feart.2022.963392

COPYRIGHT

© 2022 McIntosh, Aoki, Yanagishima,
Kobayashi, Murata and Suzuki. This is an
open-access article distributed under
the terms of the [Creative Commons
Attribution License \(CC BY\)](https://creativecommons.org/licenses/by/4.0/). The use,
distribution or reproduction in other
forums is permitted, provided the
original author(s) and the copyright
owner(s) are credited and that the
original publication in this journal is
cited, in accordance with accepted
academic practice. No use, distribution
or reproduction is permitted which does
not comply with these terms.

Reconstruction of submarine eruption processes from FTIR volatile analysis of marine tephra: Example of Oomurodasho volcano, Japan

Iona M. McIntosh^{1*}, Kaori Aoki², Taiki Yanagishima³,
Makoto Kobayashi⁴, Masanori Murata² and Takehiko Suzuki²

¹Solid Earth Geochemistry Research Group, Volcanoes and Earth's Interior Research Center, Research Institute for Marine Geodynamics, Japan Agency of Marine–Earth Science and Technology (JAMSTEC), Yokosuka, Japan, ²Research Center for Hazard Mitigation in Volcanic Islands and Urban Areas, Tokyo Metropolitan University, Tokyo, Japan, ³Soft Matter Physics Laboratory, Graduate School of Science, Kyoto University, Kyoto, Japan, ⁴Mt. Fuji World Heritage Centre, Shizuoka, Japan

Tephra layers in marine sediments are widely used to correlate and date paleoclimate and paleoceanography records, and to determine spatiotemporal changes in magmatic evolution and eruption frequency. Dissolved matrix glass H₂O contents of marine tephra could potentially inform understanding of eruption processes but are rarely used due to the issue of secondary hydration after deposition. Recent advancements in Fourier transform infrared spectroscopy (FTIR) volatile analysis have enabled reconstruction of original water contents of hydrated volcanic glasses. These new Fourier transform infrared spectroscopy analysis methods offer a new way to investigate tephra stored in marine sedimentary archives. We present a case study of the Od-1 tephra layer in marine sedimentary core C9010E, drilled ~40 km south of the Boso peninsula in Japan. This tephra was erupted by the shallow silicic submarine Oomurodasho volcano in the northern Izu–Bonin arc at ~13.5 ka. Our Fourier transform infrared spectroscopy volatile data show it has been affected by secondary hydration, with the extent of hydration controlled by grain size and porosity characteristics. Numerical modelling of low temperature hydration suggests Fourier transform infrared spectroscopy data offer an additional method for estimating eruption ages of marine tephra. OH contents, unaltered by low temperature secondary hydration, record low ambient eruptive pressures for all grain sizes and tephra types i.e., blocky and dense or pumiceous. Consideration of hydrostatic pressure gradients and past sea level at Oomurodasho shows that the majority of tephra volatile data cannot be explained by quench within a submarine eruption plume. Instead, OH contents record quench fragmentation within the shallow submarine edifice. Physical characteristics of the tephra are consistent with the formation of these tephra by explosive phreatomagmatic eruption processes. Together these OH data and tephra characteristics support the interpretation that the Od-1 tephra layer was formed by the same shallow phreatomagmatic eruption that formed the existing Oomuro Hole crater and that produced subaerial tephra deposits on nearby Izu–Oshima and Toshima

islands. This study demonstrates the crucial contribution that imaging Fourier transform infrared spectroscopy analysis can make to the interpretation of degassing and eruption processes of volcanic glasses, particularly vesicular pyroclasts and/or glasses affected by secondary hydration, adding an important new dimension to marine tephra research.

KEYWORDS

submarine volcano, tephra, FTIR volatile analysis, hydration, marine sediments, phreatomagmatic eruption, H₂O species, matrix glass

1 Introduction

Marine environments that experience continuous sedimentation and little physical or biological disturbance of seafloor sediments can create excellent archives of volcanic tephra produced by both subaerial and submarine volcanoes. In contrast to terrestrial environments, where continual erosion and reworking of volcanic deposits can erase evidence of past eruptions from the geological record, marine sedimentary archives can preserve thin tephra beds associated with small local eruptions or large but distal eruptions and even cryptotephra layers where the concentration of grains is too low to be seen by the naked eye (e.g., Ponomareva et al., 2015). Volcanic tephra comprise juvenile and lithic material ranging in size from extremely fine to coarse ash (<63 μm–2 mm; often glass shards and mineral crystals) to lapilli (2–64 mm) and blocks and bombs (>64 mm) (e.g., White and Houghton, 2006; Lowe, 2011). Marine tephra are characterized in a number of ways, including major and trace element chemistry and isotopic compositions of glass shards; heavy and light mineral assemblages; refractive indices of glass shards and heavy minerals; and morphology, color, and grain size of glass shards and larger clasts. These features have been used to identify distinctive widespread tephra of known eruption age, usually created by Plinian or Ultra-Plinian eruptions of subaerial volcanoes, that can be found in marine sedimentary cores recovered from wide geographical areas (e.g., Machida, 1999; Ikehara, 2015; Kimura et al., 2015). Such key marker tephra can be used to provide age markers when creating age models of submarine cores or correlating records from various sites (e.g., Aoki, 2008; Aoki, 2020; Candy et al., 2021); conversely, high resolution dating of marine sediments *via* ¹⁴C or ¹⁸O isotopes of calcite shells of marine organisms can be used to find depositional ages of unknown tephra, thereby reconstructing eruption records that are not preserved on land (e.g., di Roberto et al., 2020; Kutterolf et al., 2021a).

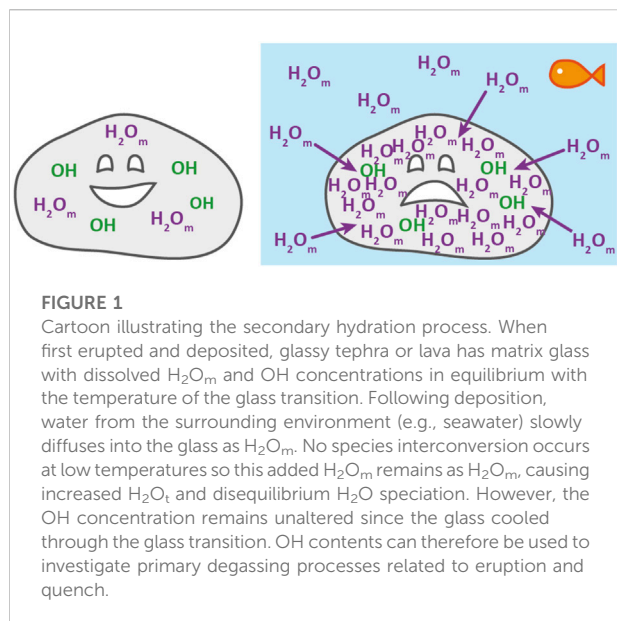
While tephrochronology and tephrostratigraphy approaches therefore make marine tephra integral to a range of paleoenvironmental and paleoceanographic studies, they also can be used to investigate volcanic processes in their own right. Analysis of tephra from sedimentary cores taken across a region can elucidate spatiotemporal changes in eruption frequency and magma compositions (e.g., Kutterolf et al.,

2018; Kutterolf et al., 2021a; Kutterolf et al., 2021b). Moreover, analysis of individual tephra beds can reveal evidence for particular eruption processes. Even if magma geochemistry is often (although not always) homogenous through individual eruptions or sequences of eruptions, physical characteristics of tephra such as vesicularity, size and morphology of grains can, in conjunction with consideration of transport and deposition processes, yield evidence for eruption styles and magnitudes (e.g., Freundt et al., 2021). For example, marine tephra deposits from the 1650 CE eruption of the submarine Kolumbo volcano in Greece contain highly vesicular grains and blocky equant grains, inferred to record primary volatile degassing during the initial subaqueous phase of the eruption and subsequent violent phreatomagmatic activity creating subaerial plumes, respectively (Fuller et al., 2018).

Marine tephra also have the potential to record crucial information about volcanic degassing processes in the dissolved magmatic volatile contents of glass shards. Since volatile solubility in magma varies with pressure and temperature, the final matrix glass volatile contents of tephra could record information about the quench of magma to glass, through fragmentation and/or cooling. H₂O is often the most volumetrically abundant magmatic volatile (particularly for silicic magmas like rhyolite) and exerts a key control on magma viscosity, the diffusivities of other volatiles and the dynamics of vesiculation and crystallization. However, original eruptive H₂O contents of marine tephra are susceptible to overprinting due to hydration of glass by external water at low temperature i.e., 'secondary hydration' (e.g., Bryant et al., 2003; Helo et al., 2011; Kutterolf et al., 2014; Ikehara et al., 2017). Recent developments in Fourier transform infrared spectroscopy (FTIR) analysis now make it possible to analyze hydrated glasses and reconstruct their primary H₂O contents. Their application to volatile analysis of hydrated pumice and lava deposits has opened up a new frontier in the investigation of submarine eruptions, which we propose in this paper can be extended to marine tephra in general.

1.1 FTIR volatile analysis

Many of the existing methods for analyzing H₂O contents of glasses, such as secondary ion mass spectrometry (SIMS),



hydrogen manometry, or thermogravimetric analysis (TGA), can only quantify the total amount of H_2O (H_2O_t) in the glass. The critical advantage of FTIR analysis is that it can also quantify the two species of water that exist in magmas and glasses. These species are molecular water (H_2O_m) and hydroxyl groups (OH). Many years of experimental studies have quantified how the proportions of H_2O_m and OH (i.e., ' H_2O speciation') vary with temperature, pressure, and H_2O_t in different magma compositions (e.g., Stolper, 1982a; Zhang, 1999; Zhang and Ni, 2010); crucially, studies have also shown that these species proportions become fixed when a sample cools through the glass transition (Dingwell and Webb, 1990; Zhang et al., 1997). The basis for reconstructing original H_2O contents of hydrated glasses is that low temperature hydration only adds H_2O_m , while OH remains unchanged (McIntosh et al., 2017; Figure 1). Accurate measurement of OH content by FTIR combined with the H_2O speciation relationships constrained from lab experiments thus enables reconstruction of original eruptive water contents of hydrated glasses.

The current breakthrough in the use of FTIR for analysis of hydrated glasses is possible because of two key advancements. The first is the use of imaging FTIR and synchrotron-source FTIR analysis, which produce spectra with a spatial resolution of a few microns, which enables analysis even of vesicular glasses like pumice that cannot be easily prepared as the double polished sample wafers of known thickness used in standard FTIR analysis (e.g., Wysoczanski and Tani, 2006; Mitchell et al., 2018; Murch, 2018; McIntosh et al., 2022; Yeo et al., 2022). The second is the species-dependent ϵ_{3500} molar absorptivity coefficient method of McIntosh et al., 2017. IR molar absorptivity coefficients (ϵ) are used in the Beer-Lambert equation that converts IR peak absorbance into concentration (e.g., Stolper, 1982b). Although it

has long been known that the value of ϵ for the mid-IR H_2O_t peak (ϵ_{3500}) varies with the proportions of H_2O_m and OH in the glass (Newman et al., 1986; Okumura et al., 2003), the near-IR H_2O_m and OH absorption peaks at $5,200\text{ cm}^{-1}$ and $4,500\text{ cm}^{-1}$ —which can confirm the proportions of H_2O_m and OH in the glass, and thus the correct ϵ_{3500} value to use—are often too weak to be detected in thin or H_2O_t -poor matrix glasses. Instead, only the mid-IR H_2O_t and H_2O_m absorption peaks at $3,500\text{ cm}^{-1}$ and $1,630\text{ cm}^{-1}$ can be detected. With no independent way to know how much OH is in the glass, previous studies of such glasses have had to choose a fixed ϵ_{3500} value from the literature to calculate H_2O_t wt% from the $3,500\text{ cm}^{-1}$ H_2O_t peak. H_2O_m wt% is calculated from the $1,630\text{ cm}^{-1}$ H_2O_m peak, and then OH wt% could be calculated as OH wt% = H_2O_t wt% - H_2O_m wt% (known as 'OH-by-difference'). Unfortunately, in many glass compositions the ϵ_{3500} value varies widely with speciation e.g., from 56 to $100\text{ L mol}^{-1}\text{ cm}^{-1}$ for rhyolites with 100% H_2O_m or 100% OH, respectively (Newman et al., 1986). This can lead to large uncertainty on the H_2O_t wt% value and therefore on the OH wt% calculated as OH-by-difference, with many hydrated glasses even appearing to have negative OH wt% values (McIntosh et al., 2017). The species-dependent ϵ_{3500} method of McIntosh et al. (2017) overcomes this issue by modifying the standard Beer-Lambert equation to use paired 'end-member' ϵ_{3500} values for the H_2O_t peak (i.e., the ϵ_{3500} values assuming 100% H_2O_m or OH in the glass), together with the known H_2O_m wt% constrained from the $1,630\text{ cm}^{-1}$ H_2O_m peak. This modified equation makes it possible to accurately calculate both H_2O_t wt% and OH wt% using only the mid-IR H_2O_t and H_2O_m absorption peaks. This improved accuracy in the OH wt% measurement is particularly crucial when using OH wt% to reconstruct the original H_2O_t wt% of hydrated glasses. Together, these advancements have therefore revolutionized the analysis of silicic submarine eruption products, because silicic glass compositions are particularly susceptible to secondary hydration (e.g. Bryant et al., 2003; Giachetti and Gonnermann, 2013), and silicic submarine eruptions often produce vesicular deposits such as pumice (e.g. Kato, 1987; Kano, 2003).

With these new FTIR techniques, H_2O speciation data from recent eruptions whose deposits are too young to have been affected by slow low temperature secondary hydration have helped reveal primary eruption processes. For example, the paradigm-shifting eruption of Havre volcano in the Kermadec arc in 2012 showed unequivocally that a deep-sea ($\sim 900\text{ m}$ water depth) eruption could produce floating pumice at the sea surface (Carey et al., 2014; Carey et al., 2018). FTIR analysis of the raft pumice and other highly vesicular seafloor pumice revealed that clasts had cooled slowly during buoyant ascent within a submarine plume, enabling continued degassing to shallow pressures and subsequent syn-eruptive hydration during cooling (Mitchell et al., 2018). Conversely, analysis of vesicular dacite lava from the 2019 submarine to emergent effusive eruption of Late'iki (formerly known as Metis Shoal) in the

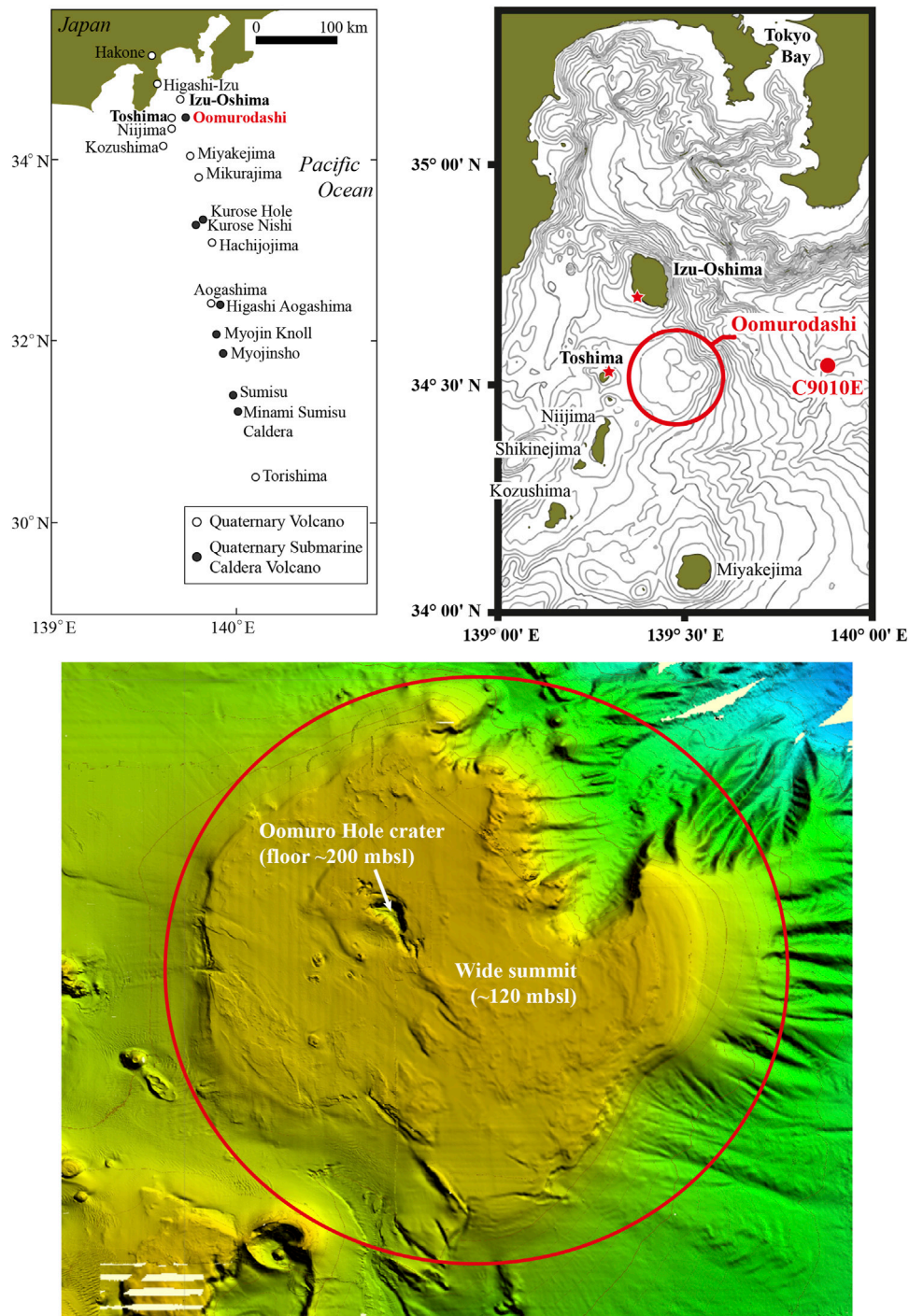


FIGURE 2
 Location of the shallow submarine Oomurodashi volcano in the northern Izu-Bonin arc. Bathymetry collected during cruises NT12-19 of *R/V Natsushima* and KS-16-6 of *R/V Shinsei-maru*. Red circle encompasses the broad Oomurodashi edifice. The small Oomuro Hole crater is located in the wide flat summit area and hosts an active hydrothermal field. Red dot indicates location of the C9010E core drilled by *D/V Chikyū*. Red stars indicate location of subaerial tephra layers O58 on Izu-Oshima and O3T on Toshima islands.

Kingdom of Tonga showed that the vesicular lavas in this island-forming eruption degassed to atmospheric pressure and exhibit no syn-eruptive hydration (Yeo et al., 2022). Together these

constraints from recent eruptions provide the beginnings of a volatile-based framework for interpreting the degassing and eruption processes of older, unobserved submarine eruptions.

This FTIR volatile approach was therefore recently used to investigate the late Quaternary submarine and subaerial deposits of Oomurodashī, a shallow silicic volcano in the northern Izu-Bonin arc that lies 60 km from the entrance to Tokyo Bay (McIntosh et al., 2022). H₂O speciation data revealed that both submarine and subaerial deposits had been affected by secondary hydration in the time since eruption, so OH contents were used to interpret eruption processes. OH contents of *in situ* vesicular submarine lavas were used to estimate the ambient pressure (i.e., water depth) at the time of their emplacement; interpreting these pressures in the context of past sea level rise made it possible to estimate eruption ages for these young submarine lavas for which other typical geological dating methods (such as radiocarbon dating) cannot be applied. They also used OH contents of pumiceous submarine deposits to determine their quench depths within the overlying water column, and showed that OH contents of pumice in subaerial tephra deposits provide additional evidence that these deposits were formed by explosive phreatomagmatic activity within the shallow submarine edifice.

In this work we return to the case study of Oomurodashī volcano in order to highlight how FTIR H₂O speciation data can be used to investigate tephra in marine sedimentary archives, which are commonly affected by secondary hydration. Here we focus on a tephra layer from a marine sedimentary core collected ~45 km east of Oomurodashī that has been geochemically fingerprinted as being from Oomurodashī. We present matrix glass volatile contents and physical characteristics of this tephra and investigate its relation to other known eruption deposits from Oomurodashī. With this study we demonstrate how H₂O speciation data can be used not only to identify and link tephra layers in sedimentary archives, but also to investigate the fundamental eruption processes that generated them.

1.2 Geological setting

Oomurodashī volcano is located in the northern Izu-Bonin volcanic arc, which is an intra-oceanic convergent margin formed by the westward subduction of the Pacific Plate beneath the Philippine Sea Plate (Figure 2). In this section of the arc, the volcanic front is characterized by volcanic islands that erupt predominantly basaltic compositions interspersed with submarine volcanoes that erupt predominantly silicic compositions (e.g., Yuasa et al., 1991; Taylor, 1992; Tamura and Tatsumi, 2002). Many of these submarine silicic volcanoes have formed calderas and are thought, on the basis of seafloor surveys and regional marine sedimentary deposits, to have produced prodigious amounts of silicic pyroclastic material throughout the Quaternary (e.g., Nishimura et al., 1992; Fiske et al., 2001; Yuasa and Kano, 2003; Tani et al., 2008; Allen et al., 2010). Documented eruptions in historical times include an eruption of Sumisujima in 1916 (Ito) and multiple eruptions

of Myojinsho including a 1952 eruption that destroyed an investigating Japanese research vessel (Morimoto and Ossaka, 1955; Fiske et al., 1998), with its most recent confirmed eruption being in 1970 (Ito). Frequent reports of discolored water and sulfurous odor suggest that additional unobserved submarine activity is likely occurring at these and other volcanoes along the arc. In this context, the shallow silicic submarine Oomurodashī volcano is of particular interest. Although previously thought to be inactive, the discovery in 2012 that it hosts an active shallow hydrothermal field (Tani et al., 2013) and its location at shallow depths close to inhabited coastlines and major shipping lanes approaching Tokyo Bay has emphasized the need to constrain its past eruptions and the likelihood of hazardous volcanic activity in the future.

Oomurodashī has a wide edifice with a ~20 km diameter flat summit that lies at ~120 m below sea level (m b.s.l.) (Figure 2), which is thought to have been created by wave planation during the low sea level stand at the time of the Last Glacial Maximum (Hamuro et al., 1983; Yuasa et al., 1991). In the approximate center of this flat summit is a small crater (~1.2 x 0.7 km, ~80 m deep) called Oomuro Hole. Surveys by the research vessels *R/V Natsushima* (cruises NT07-15, NT12-19) and *R/V Shinseimaru* (cruise KS-16-6) collected bathymetry data and conducted seafloor observations and sampling using a remotely operated vehicle (ROV). These surveys identified an active hydrothermal field in the bottom of the Oomuro Hole crater and documented and sampled eruption deposits from the shallow submarine edifice, including fresh rhyolite lavas and pumice from the walls of Oomuro Hole and the surrounding summit area (Tani et al., 2013).

Geochemical data for these rhyolites sampled from the submarine Oomurodashī edifice are published in McIntosh et al. (2022). Based on these geochemical data, the authors established that Oomurodashī is the source of two subaerial tephra deposits on nearby islands (Figure 2). Layer O58 (Uesugi et al., 1994) on Izu-Oshima, ~20 km northwest of Oomurodashī, has a published ¹⁴C age of 13.4 ka (Saito and Miyairi, 2008), while layer O3T on Toshima, ~15 km west of Oomurodashī, lies between layers dated to 11 and 15 ka (Oikawa and Tani, 2020). The published ¹⁴C age for layer O58 was produced using the now outdated IntCal04 (Reimer et al., 2004) and OxCal ver3.10 (Bronk Ramsey, 2005) models; recalculating the age from the data of Saito and Miyairi (2008) using the most recent versions (IntCal20, Reimer et al., 2020; OxCal ver4.4.4 Bronk Ramsey, 2021), gives an age of 13.5 ka. Both the O58 and O3T tephra layers have a distinctive appearance with sparse white pumice clasts, generally <1 cm but up to 4 cm in size, dotted throughout dark fine-grained matrix material. Based on tephra characteristics including particles with stepped fractures indicative of brittle fragmentation by magma-water interaction, particles with partial manganese coatings likely formed in the submarine environment, and dense angular lithics in the base of the O58 layer, these subaerial deposits are proposed to result

from the explosive formation of the Oomuro Hole crater by a shallow submarine, phreatomagmatic eruption (McIntosh et al., 2022).

Tephra from this 13.5 ka subaerial eruption would also have been deposited in the marine environment, and potentially preserved in the local marine sediment record. Marine sedimentary core C9010E was drilled by the drilling vessel *D/V Chikyu* in 2009 at 34°33.46'N, 139°53.38'E, in a water depth of 2,027 m, ~45 km to the east of Oomuro Hole (Figure 2). This core contains multiple tephra deposits from volcanoes in the northern Izu-Bonin arc, which are described in detail in Aoki et al. (2020), (2019). One of these layers, Od-1, has been identified on the basis of geochemistry as being an eruption deposit of Oomurodashi (Aoki et al., 2019; Takahashi et al., 2022). This layer occurs between 16.722–16.772 m below sea floor (m b.s.f.), and is located between tephra correlated to the Miyatsukayama event (Nj-Mt tephra, 12.8 ka BP (Kobayashi et al., 2020)) and Akazakinomine events (Nj-AkG tephra series, ~15–20 ka BP (Kobayashi et al., 2020)) from Niiijima volcano (Aoki et al., 2019; Takahashi et al., 2022). Od-1 is also the only tephra since the start of the Akazakinomine events (i.e., in sediments younger than 20 ka BP) that matches the geochemistry of Oomurodashi (Aoki et al., 2019). From this we infer that the Od-1 layer in the C9010E core is most likely coeval with the 13.5 ka subaerial O58 and O3T layers on Izu-Oshima and Toshima. In this study, we further explore this hypothesis through analysis of the physical characteristics and dissolved volatile contents of the Od-1 tephra.

2 Methods

2.1 Tephra sampling

Tephra samples were washed in fresh water using an ultrasonic bath. After decanting, they were left to dry at room temperature and then sieved using mesh diameters of 250, 125 and 63 μm .

2.2 Imaging Fourier transform infrared spectroscopy (FTIR) analysis

For FTIR analysis of dissolved volatiles in glass, samples are usually prepared as free-standing parallel-polished wafers of known thickness. This was attempted but ultimately unsuccessful due to the small size and colorless glass of the tephra grains, which increased the likelihood of sample loss during grinding, polishing and turning; and due to their relatively high vesicularity and the difficulty of fully removing the Crystalbond 509 resin used during wafer preparation. This resin dissolves in acetone but experience shows that it (and other similar resins) is difficult to fully remove from vesicular samples, leaving a small contamination peak at ~1,730 cm^{-1} in FTIR

spectra that interferes with the measurement of the 1,630 cm^{-1} $\text{H}_2\text{O}_\text{m}$ absorption peak (McIntosh et al., 2022). Tephra grains were therefore analyzed without double polishing. For the <250 μm size fractions individual grains were picked out and directly placed on the sample holder for analysis (i.e., without any polishing at all). Larger clasts from the >250 μm fraction were lightly crushed to produce thinner glass shards that could then be picked and analyzed.

Imaging FTIR analyses were conducted at JAMSTEC using a Varian FTS Stingray 7000 Micro Imager Analyzer spectrometer with an attached UMA 600 microscope. The spectrometer was operated under a N_2 gas purge to reduce atmospheric interference. Images were collected in the mid-IR range (6,000–700 cm^{-1}) at a spectral resolution of 8 cm^{-1} using a ceramic (globar) infrared source, a Ge-coated KBr beamsplitter, and a liquid nitrogen-cooled Varian Inc. Lancer Focal Plane Array (FPA) camera housed in the microscope. The FPA camera consists of 4,096 infrared photovoltaic HgCdTe_2 (MCT) detector pixels arranged in a 64 x 64 grid that image a 350 x 350 μm sample area, producing a pixel spatial resolution of ~5.5 x 5.5 μm . The FPA camera was calibrated regularly. Samples were placed on an IR-transparent KBr window for analysis. An initial background IR image of the KBr window was collected and then automatically subtracted from each sample image; new background images were taken approximately every 2 h. Each image (comprising 512 scans) takes ~15 min to acquire. Each tephra grain or glass shard was imaged in transmission mode and then reflectance mode (without moving the stage) before moving to the next grain to be analyzed.

Images were processed using the Varian Win-IR Pro software (v3.3.1.014). To quantify volatile concentrations from IR absorbance peaks it is necessary to know the thickness of the sample glass. For these small unpolished grains it would not be possible to accurately constrain thickness variation across the IR image using digital micrometer measurements. Instead, individual pixels within the IR images that yielded good spectra in both transmission and reflectance were selected and processed as individual spot analyses with ~5.5 x 5.5 μm resolution (Figure 3). Glass thickness for each spot was then calculated from the frequency of interference fringes in the reflectance spectra (e.g., Wysoczanski and Tani, 2006; Nichols and Wysoczanski, 2007), using a refractive index of 1.5 for rhyolite glass (Long and Friedman, 1968). Above a certain thickness (roughly 150 μm for unpolished samples) this method cannot be used because reliable interference fringes do not form. For this reason, imaging analyses of grains from the 125–250 μm size fraction were unsuccessful due to the lack of interference fringes for thickness measurement. Although some IR images of grains and shards from the smaller size fractions and crushed larger clasts also contained insufficient pixels with suitable interference fringes for successful analysis, the majority of imaged grains could be successfully processed. For individual pixel locations where glass thickness could be

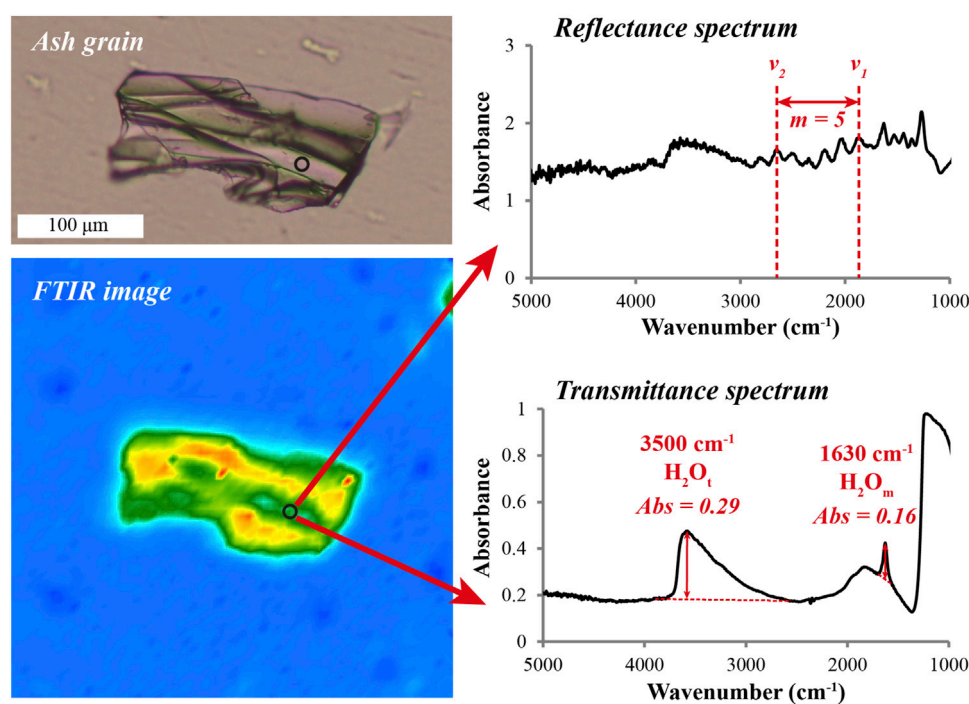


FIGURE 3

Example of imaging FTIR analysis of tephra. Transmitted light photograph of unpolished pumiceous ash grain. Tephra grains are then analyzed by imaging FTIR in both reflectance and transmittance modes. FTIR images are $350 \times 350 \mu\text{m}$, comprising 64×64 individual spectra with spatial resolution $\sim 5.5 \times 5.5 \mu\text{m}$. The same pixel (spectrum location) is selected from both images for processing. The reflectance spectrum is used to find glass thickness from the distance between interference fringes (whose wavelength varies according to glass thickness and refractive index) via the method of Nichols and Wysoczanski (2007). The transmittance spectrum is used to find H_2O_m and H_2O_t absorbance by measuring peak height above a baseline. Despite unpolished surfaces, Od-1 tephra spectra are well fit by linear baselines.

constrained from fringes in the reflectance spectrum, volatile absorbance was then obtained from the corresponding transmission spectrum by measuring the peak height above a baseline (Figure 3).

The combination of thin glasses and the decreasing sensitivity of the imaging detector at high wavenumbers meant that the near-IR $5,200 \text{ cm}^{-1}$ H_2O_m and $4,500 \text{ cm}^{-1}$ OH absorbance peaks could not be measured; instead, water concentration and speciation were constrained using the mid-IR $3,500 \text{ cm}^{-1}$ H_2O_t and $1,630 \text{ cm}^{-1}$ H_2O_m absorbance peaks. Non-parallel glass and proximity to bubble walls can cause curving, non-linear baselines that require flexicurve baselines (e.g., McIntosh et al., 2022), however most spectra could be well fit with a linear baseline with tie points individually adjusted for each spectrum. Typical tie points were $3,930$ and $2,589 \text{ cm}^{-1}$ for the H_2O_t peak and $1,695$ and $1,563 \text{ cm}^{-1}$ for the H_2O_m peak; adjustments were made when necessary to avoid the baseline position falling on an arbitrarily high or low position related to noise or interference fringes. For H_2O_t a peak position of $3,570 \text{ cm}^{-1}$ was appropriate for all spectra; for H_2O_m the peak position varied from $1,621$ – $1,633 \text{ cm}^{-1}$ with the majority (275 out of 368 spectra; 75%) having a peak position of $1,628 \text{ cm}^{-1}$. H_2O_m

concentrations were calculated in the standard manner by entering measured peak absorbances and glass thicknesses into the Beer-Lambert law (Stolper, 1982a), using a molar absorptivity coefficient for the $1,630 \text{ cm}^{-1}$ H_2O_m peak in rhyolite of $55 \pm 2 \text{ L mol}^{-1} \text{ cm}^{-1}$ (Newman et al., 1986). The $3,500 \text{ cm}^{-1}$ H_2O_t absorbance peak requires a molar absorptivity coefficient (ϵ) that varies according to the proportions of H_2O_m and OH dissolved in the glass (Newman et al., 1986). H_2O_t and OH concentrations were therefore calculated using the modified Beer-Lambert law method of McIntosh et al. (2017), which accounts for the species dependence of the $3,500 \text{ cm}^{-1}$ H_2O_t molar absorptivity coefficient ϵ_{3500} . CO_2 was below detection limits for all samples. Detection limits are inversely proportional to sample thickness. For the mean thickness of the thickest glass shard ($45 \mu\text{m}$) the CO_2 detection limit is ~ 7 ppm, assuming a minimum absorbance of 0.005 and using a molar absorptivity value of $1,214 \text{ L mol}^{-1} \text{ cm}^{-1}$ for the $2,350 \text{ cm}^{-1}$ CO_2 peak (Behrens et al., 2004); for a $20 \mu\text{m}$ thickness this detection limit would increase to ~ 16 ppm.

Both the standard and modified Beer-Lambert law methods require a value for glass density, which can be calculated from the

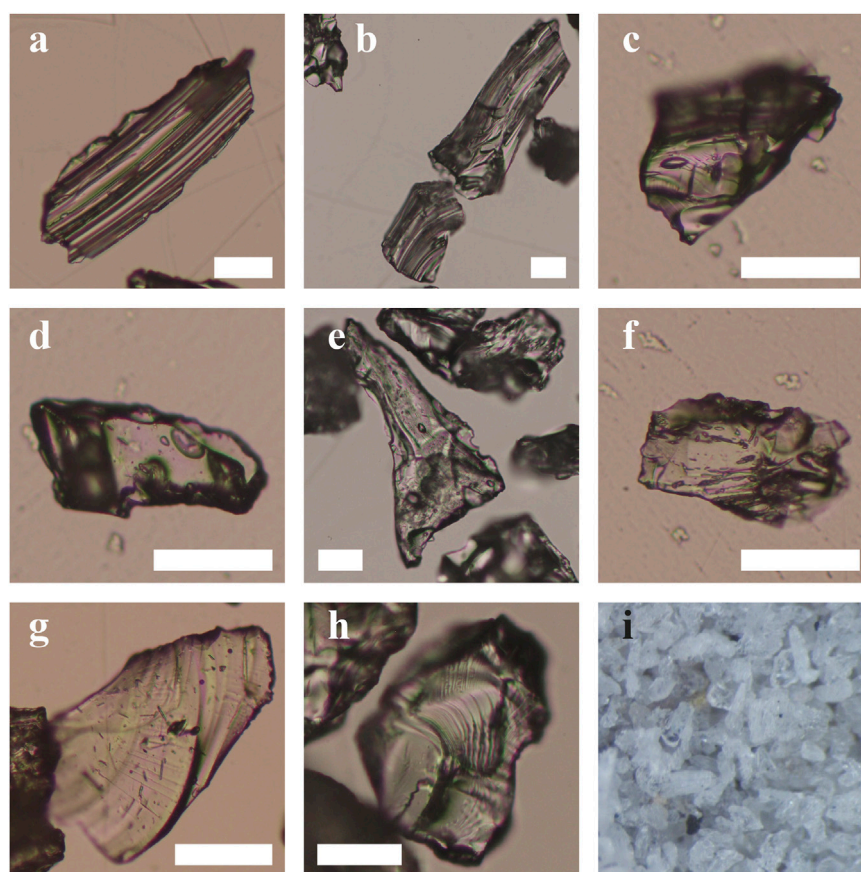


FIGURE 4

Transmitted light photographs of tephra types (all taken from the 63–125 μm size fraction). White scalebars represent 50 μm . (A,B) pumiceous shards; (C,D) dense/blocky shards; (E) rare microlite-rich shard; (F) rare dense shard with distorted, possibly collapsing, vesicles; (G,H) shards with brittle stepped fractures on surfaces; (I) bulk sample of 63–125 μm size fraction.

major element chemistry (Lange and Carmichael, 1987) and dissolved H_2O_t content (Ochs and Lange, 1997) of the glass. Appropriate values of glass density were therefore calculated iteratively, by adjusting the H_2O_t wt% used in the glass density calculation until the resulting glass density value produced the same H_2O_t wt% in the FTIR concentration calculations. Major element data were based on the published geochemistry of the O58 and O3T pumice clasts (McIntosh et al., 2022). For this glass chemistry, an anhydrous composition would have a glass density of 2,415 g/L while a dissolved H_2O_t content of 2 wt% would reduce glass density to 2,379 g/L. The dependence of calculated FTIR H_2O contents on glass density is however relatively weak. For example, the average calculated H_2O_t wt% of the most water-rich size fraction only varies from 1.83 to 1.88 wt% for input glass density values spanning 2,415 to 2,350 g/L, respectively. We therefore chose to simplify the iterative calculations by using the average H_2O_t wt% of each size fraction to calculate a fixed glass density value for that size fraction, being 2,381, 2,385, 2,388 and 2,403 g/L for the

0–63 μm , 63–125 μm , >250 μm pumice and >250 μm dense clast size fractions, respectively.

The largest error on FTIR concentrations for thin glasses is usually derived from the error on determining glass thickness from reflectance spectra, typically reported as $\pm 3 \mu\text{m}$ (Nichols and Wysoczanski, 2007), which can give errors of $\pm 15\%$ relative for thin (<20 μm) glasses. The non-linear baselines of some of the transmission spectra create additional uncertainty when measuring the peak absorbances. However, comparison of linear and non-linear baselines for these spectra finds that the difference in measured peak height is minor and can be considered negligible for these spectra where peak absorbances are typically >0.1. Errors on volatile concentrations for each spectrum are therefore considered to fall within the error resulting from the $\pm 3 \mu\text{m}$ error on the thickness measurement. Multiple pixel spots were analyzed per tephra grain (typically 10 pixels per grain) or clast (20–30 pixels from multiple shards). Volatile data are presented as the mean value of all pixel spot measurements for each grain

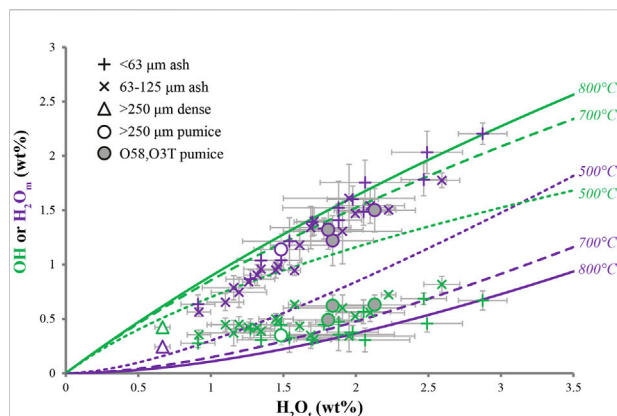


FIGURE 5

FTIR H₂O species data for the Od-1 tephra. Mean OH (green) and H₂O_m (purple) concentrations plotted against mean H₂O_t concentration for each tephra grain or clast. Error bars show \pm two times the standard error of the mean. Symbols indicate grain size fraction. Grey symbols are data for subaerial pumice clasts in the subaerial O58 and O3T deposits reported in McIntosh et al. (2022). Curves show expected OH (green) and H₂O_m (purple) concentrations for a given H₂O_t concentration assuming equilibrium speciation for temperatures of 800°C (solid line), 700°C (dashed line) and 500°C (dotted line). Curves calculated using the H₂O speciation model of Nowak and Behrens (2001) for rhyolite. Measured species concentrations do not lie on these equilibrium curves, indicating disequilibrium speciation.

or clast. Errors are given as \pm two times the standard error of the mean.

3 Results

3.1 Tephra description

The Od-1 tephra is predominantly composed of 63–250 μ m vitric ash shards, accompanied by finely vesicular gray to beige pumice with a maximum grain size of 7 mm. Quartz, beta-quartz, feldspar, and orthopyroxene minerals are also observed. Two distinct types of glassy tephra were seen across all grain size fractions (Figure 4). One tephra type is made of dense and blocky grains. These contain small, isolated bubbles, which may range from spherical to moderately aligned, or appear partially collapsed or resorbed. Some of these blocky grains contain microlites while others are microlite-free. These blocky grains may display repeated step-like fractures of their outer surfaces. The second tephra type is a ‘pumiceous’ type, where grains exhibit strongly elongated and aligned bubbles. These bubbles often extend beyond the edges of the individual grains, showing that they are fragments of larger pumiceous material. This pumiceous grain type does not contain microlites and no step-like features are seen on their outer surfaces. Larger clasts in the >250 μ m fraction can also be classified into dense and pumiceous types. When lightly crushed to produce suitably thin

glass shards for FTIR analysis, the resulting shards of each type have similar characteristics to the dense/blocky and pumiceous types identified in the smaller grain size fractions.

3.2 FTIR volatile data

FTIR data for the Od-1 tephra are displayed in Figure 5 and Table 1 as mean values for individual grains and clasts. Data for all individual spectra are given in the Supplementary Material. No processed spectra were excluded when calculating shard averages. This includes 4 (of a total of 368) spectra that yielded apparent negative values of OH concentration. This occurs when the measured H₂O_m absorbance is greater than the H₂O_t absorbance, which is most likely to happen due to baseline choices in glasses that contain predominantly H₂O_m. These spectra were reviewed but there was no obvious reason to reject the baseline choices. These spectra occurred in different shards. Sometimes the negative OH value was much lower than other analyses on the same grain, but not always. If excluded, calculated OH contents would change by less than 0.02 wt% and H₂O_m contents would be unaffected. It was also noted that the peak position of the (nominally 1,630 cm⁻¹) H₂O_m peak ranged from 1,621–1,633 cm⁻¹. Filtering data to exclude spectra with H₂O_m peak positions outside the range 1,626–1,630 cm⁻¹ (31 of 368 spectra) would only alter OH contents by <0.03 wt% and H₂O_m by <0.05 wt%, and would reduce the number of negative OH spectra from 4 to 2. Such spectra with peak positions outside the 1,626–1,630 cm⁻¹ range occur in a range of grains with no pattern observed in peak position with grain size, grain type, or glass thickness. Due to the negligible impacts of excluding these spectra and a desire to avoid any bias e.g., away from low OH content glasses that are more likely to yield apparent negative OH values, it was decided to present the full dataset without removing these few spectra.

Table 1 includes the values for the species-dependent ϵ_{3500} molar absorptivity coefficients resulting from the calculation method of McIntosh et al. (2017). With the exception of the >250 μ m dense clast ($\epsilon_{3500} = 84$), ϵ_{3500} is <74 for all samples. This is lower than even the lowest published fixed value of ϵ_{3500} for rhyolite glasses (75; Okumura et al., 2003) and indicates that the ratio of H₂O_m to OH in these analyzed glasses is higher than for the experimental glasses used to constrain published fixed ϵ_{3500} values. OH contents for all grains and clasts range from 0.28 to 0.82 wt%, while H₂O_m contents range from 0.24 to 2.20 wt%. Except for the >250 μ m dense clast, all samples contain more H₂O_m than OH.

Figure 5 shows mean OH (green) and H₂O_m (purple) content of each grain or clast plotted against their mean H₂O_t content. Plotted curves mark the proportions of OH and H₂O_m expected for a given H₂O_t content under equilibrium speciation conditions

TABLE 1 FTIR data for Od-1 tephra according to size fraction. Tephra type shown as D (dense/blocky) and P (pumiceous). ϵ_{3500} is the value of the species-dependent molar absorptivity coefficient for the $3,500\text{ cm}^{-1}$ H_2O_t IR absorbance peak derived according to the method of McIntosh et al. (2017). Thickness given in μm .

Shard name	Tephra type	no. spectra	Average					Two times the standard error of the mean				
			H_2O_m wt%	OH wt%	H_2O_t wt%	ϵ_{3500}	Thickness	H_2O_m wt%	OH wt%	H_2O_t wt%	ϵ_{3500}	Thickness
< 63 μm fraction												
a	D	10	1.33	0.45	1.78	67.2	24	0.10	0.02	0.10	0.7	0.8
c-RH	D	10	1.04	0.31	1.35	65.9	15	0.11	0.06	0.16	0.9	0.5
c-LH	D	8	2.03	0.46	2.49	64.0	8	0.19	0.08	0.24	0.9	0.6
d	D	8	1.76	0.31	2.06	62.1	9	0.20	0.11	0.31	1.9	1.0
e	P	10	1.49	0.57	2.05	68.0	20	0.12	0.11	0.19	1.8	0.7
f	D	8	1.52	0.36	1.88	63.2	16	0.24	0.15	0.38	3.2	0.7
g	D	8	1.39	0.31	1.70	64.0	15	0.13	0.04	0.13	1.2	1.4
h	D	10	0.64	0.28	0.91	69.3	24	0.09	0.04	0.12	0.9	1.1
i	D	10	1.41	0.47	1.88	67.2	18	0.15	0.02	0.16	0.9	0.5
j	P	7	1.21	0.33	1.54	64.7	13	0.22	0.13	0.32	2.6	1.5
k	P	8	0.87	0.41	1.27	69.6	26	0.08	0.09	0.17	2.4	0.4
l	D	11	1.78	0.69	2.47	68.3	17	0.15	0.05	0.16	1.0	0.8
p	P	10	1.60	0.38	1.98	64.3	15	0.12	0.06	0.18	0.7	1.0
q	P	10	2.20	0.67	2.87	66.2	9	0.10	0.09	0.17	0.9	0.1
t	D	10	1.04	0.45	1.49	69.0	26	0.07	0.09	0.14	1.4	0.6
63-125 μm fraction												
b	D	10	1.31	0.60	1.91	70.2	24	0.30	0.12	0.41	1.4	6.0
c	P	10	0.96	0.39	1.35	68.4	28	0.07	0.08	0.12	1.9	3.5
d	P	10	1.18	0.43	1.61	67.9	21	0.16	0.05	0.20	1.0	1.9
e	D	10	0.56	0.35	0.92	72.9	33	0.04	0.04	0.08	0.8	2.6
f	P	10	1.34	0.35	1.69	64.5	11	0.20	0.12	0.28	3.0	2.2
g	D	8	0.65	0.45	1.10	73.8	45	0.08	0.06	0.13	1.2	5.7
h	P	10	1.54	0.56	2.10	67.6	12	0.16	0.08	0.24	0.6	0.8

(Continued on following page)

TABLE 1 (Continued) FTIR data for Od-1 tephra according to size fraction. Tephra type shown as D (dense/blocky) and P (pumiceous). ϵ_{3500} is the value of the species-dependent molar absorptivity coefficient for the $3,500\text{ cm}^{-1}$ H_2O_t IR absorbance peak derived according to the method of McIntosh et al. (2017). Thickness given in μm .

Shard name	Tephra type	no. spectra	Average					Two times the standard error of the mean				
			H_2O_m wt%	OH wt%	H_2O_t wt%	ϵ_{3500}	Thickness	H_2O_m wt%	OH wt%	H_2O_t wt%	ϵ_{3500}	Thickness
i	P	10	1.78	0.82	2.59	69.8	20	0.07	0.07	0.12	0.7	1.2
j	P	10	1.61	0.34	1.95	62.4	16	0.31	0.14	0.45	2.6	1.5
k	P	10	0.90	0.42	1.32	70.0	32	0.10	0.03	0.09	1.4	1.1
n	P	10	1.40	0.31	1.71	64.1	13	0.13	0.04	0.12	1.2	1.4
o	P	10	1.47	0.52	2.00	67.6	19	0.03	0.01	0.04	0.2	0.3
p	D	10	0.95	0.50	1.45	71.2	21	0.07	0.05	0.12	0.6	1.7
q	P	8	0.84	0.42	1.26	70.6	28	0.01	0.05	0.04	1.3	0.5
r	D	10	1.50	0.72	2.23	70.3	28	0.05	0.02	0.05	0.4	0.8
s	D	8	0.79	0.37	1.16	69.5	25	0.11	0.12	0.22	2.2	2.8
u	D	12	0.94	0.63	1.58	73.7	27	0.04	0.02	0.04	0.7	0.9
v	D	9	0.98	0.48	1.46	70.4	26	0.03	0.02	0.04	0.4	0.5
w	D	8	0.74	0.45	1.19	72.6	35	0.14	0.07	0.19	1.3	5.0
> 250 μm clasts												
Dense	D	19	0.24	0.42	0.67	83.9	17	0.02	0.04	0.05	0.9	2.3
Pumice	P	29	1.14	0.35	1.49	66.1	12	0.15	0.09	0.19	1.9	1.9

in rhyolite for temperatures of 500, 700 and 800°C (Nowak and Behrens, 2001). No samples plot within these curves, indicating that their species concentrations are not in equilibrium with temperatures of 500–800°C.

4 Discussion

4.1 Cause of observed disequilibrium H₂O speciation

At magmatic temperatures H₂O_m and OH interconvert according to the reaction:



in which H₂O_m reacts with bridging oxygen atoms (O^o) to produce OH groups that are bound to the silicate framework (Stolper, 1982b). The equilibrium position of this reaction varies with H₂O_t content and temperature (Stolper, 1982a; Zhang et al., 1997; Zhang, 1999; Nowak and Behrens, 2001). At low H₂O_t contents OH is the dominant species, but as H₂O_t increases the equilibrium position shifts toward the left and the proportion of H₂O_m increases so that H₂O_m becomes the dominant species at higher H₂O_t contents (see curves in Figure 5). Meanwhile, the reaction also shifts towards the right (more OH) at higher temperatures and towards the left (more H₂O_m) at lower temperatures. Thus for a given H₂O_t content there should be more OH and less H₂O_m at higher temperatures (Figure 5).

When magma is erupted and begins to cool, its OH content will begin to decrease and its H₂O_m content will begin to increase as the equilibrium position of the interconversion reaction shifts toward the left with decreasing temperature. However, the rate of this interconversion reaction is strongly temperature dependent and decreases dramatically with temperature (Zhang et al., 1991; Zhang et al., 1995). It therefore takes an increasingly long time for OH to interconvert to H₂O_m as the erupted magma cools. When a certain temperature is reached, the reaction rate becomes negligible and there is no further interconversion with further cooling i.e., the concentrations of H₂O_m and OH become fixed. This temperature is termed the temperature of apparent equilibrium, *T_{ae}* (Zhang, 1994).

T_{ae} is closely related to the glass transition i.e., the transition between fluid behavior (with a viscous response to stress) and glassy behavior (with an elastic response to stress) (Dingwell and Webb, 1990, 1989). The transition from fluid to glass is controlled by the relaxation timescale of the silicate structure, which is related to the shear viscosity of the melt and thus to temperature (hence the timescale increases as the melt becomes increasingly viscous with cooling e.g., Dingwell and Webb, 1989) and H₂O_t content of the melt (due to the H₂O_t-dependence of viscosity e.g., Hess and Dingwell, 1996). When a melt is cooled the silicate structure becomes increasingly unable to relax to equilibrium until it crosses the glass transition and its final

silicate structure becomes frozen in. Faster cooling provides less time for structural relaxation so the glass transition is reached at a higher temperature (and lower viscosity) than for slower cooling; meanwhile, at the same cooling rate a low H₂O_t melt will reach the glass transition at a higher temperature than a high H₂O_t melt (e.g., Dingwell and Webb, 1989; Stevenson et al., 1995; Giordano et al., 2005). The transition from fluid to glassy behavior occurs over a temperature interval that depending on definition may span several tens of degrees (e.g., Giordano et al., 2005), but many studies define a specific glass transition temperature, *T_g*. This *T_g* value is most strictly defined as the glass transition temperature for a melt under a specific set of experimental conditions and timescales (Dingwell and Webb, 1989; Giordano et al., 2005). Importantly, *T_{ae}* has been shown to be equivalent to a rheologically-defined *T_g*, where *T_g* is the temperature at which melt viscosity is 10^{11.45}/*q*, where *q* is the quench rate in K/s; thus *T_g* is reached for a cooling rate of 10 K/min when melt viscosity is ~10¹² Pa s (Dingwell and Webb, 1990; Zhang et al., 1997; Zhang et al., 2003; Zhang and Ni, 2010). For this reason, H₂O_m and OH concentrations of volcanic glasses measured by FTIR can be compared with H₂O speciation models for the same geochemical composition (i.e., models of how H₂O species concentrations vary with H₂O_t at different equilibrium temperatures) to find the *T_{ae}*, hence *T_g*, of the sample (e.g., Zhang et al., 2000; Xu and Zhang, 2002; Wallace et al., 2003). In such cases, on a plot of H₂O_m and OH concentrations against H₂O_t concentration the sample data should fall on equilibrium speciation curves for temperatures equivalent to *T_{ae}* hence *T_g*. However, even a wide *T_g* range of 800°C (i.e., instant quench of a magma erupted at 800°C) to 500°C (requiring slow cooling of an H₂O_t-rich magma) does not encompass the observed speciation data for the Od-1 tephra (Figure 5).

T_g (hence *T_{ae}* recorded by H₂O speciation) of the Od-1 tephra will have been determined by its original H₂O_t content, its cooling rate, and the degree of deformation (strain) during its formation. By considering these related factors we can estimate a feasible *T_g* range that could have applied to the Od-1 tephra, against which we can interpret their FTIR data. The low OH contents of the tephra (mean 0.45 wt% for all grains) indicate that they had degassed to relatively low pressure with correspondingly low H₂O_t contents. The H₂O speciation model for rhyolite of Nowak and Behrens (2001) shows that at 800°C 0.45 wt% OH would correspond to ~0.5 wt% H₂O_t, and even at 500°C would only correspond to ~0.6 wt% H₂O_t. The melt was therefore relatively H₂O_t-poor, which would be associated with higher *T_g*. Cooling rate will be determined by grain size and their formation and deposition history. The tephra grains are small, with most taken from the <125 μm size fractions, and would have therefore cooled rapidly whether in a submarine or subaerial eruption plume (e.g., possible quench rates of ~10–100 K/s in air or ~100–10⁶ K/s in water, Xu and Zhang, 2002; Potuzak et al., 2008; Helo et al., 2013; Moitra et al., 2020, 2018). These high cooling rates, and the high strain rates associated with tephra

formation *via* explosive fragmentation, would also favor high T_g . A low T_{ae} could still be caused for such glasses if they had a complex thermal history that involved thermal buffering at temperatures around the glass transition, which could provide time for further structural relaxation and interconversion of H_2O species. Examples include rheomorphic flows formed by accumulation and annealing of spatter deposits (Gottsmann and Dingwell, 2001; Gottsmann and Dingwell, 2002) or hyaloclastite glasses formed by rapid quench in water but subsequently buffered by heat from hot underlying lava flow interiors (Wilding et al., 2000). The Od-1 tephra however is inferred to be fallout from a subaerial plume that were deposited cold far from any volcanic vents, and there is no evidence from the sediment core for any later volcanic events that could have caused subsequent reheating of the deposits. Accordingly, we estimate that a T_g range of 800–700°C is feasible for the Od-1 tephra. That the observed speciation data do not fall in this range indicates that the tephra have ‘disequilibrium speciation’. This disequilibrium speciation could be caused by 1) quench resorption of bubbles within the magma during cooling, 2) syn-eruptive hydration by external water occurring at intermediate temperatures during cooling in a plume, or 3) secondary hydration by external water occurring at low temperature in the time following deposition on the seafloor.

Quench resorption occurs when the increase in H_2O_t solubility in silicate melts with decreasing temperature causes exsolved magmatic water vapor within bubbles to re-dissolve in the melt as erupted magma cools (McIntosh et al., 2014). This can create disequilibrium speciation because the resorbing vapor is added as H_2O_m , some amount of which must then be interconverted to OH to attain equilibrium speciation for the temperature and H_2O_t conditions. If cooling is sufficiently rapid, the dramatic decrease with temperature of the species interconversion reaction rate prevents significant interconversion of newly added H_2O_m before the glass transition is crossed and species proportions become fixed, resulting in ‘excess’ H_2O_m and disequilibrium H_2O speciation in the diffusion profile surrounding resorbing bubbles. This was observed by McIntosh et al. (2014) in high pressure experimental samples containing several wt% of H_2O_t , where rapid H_2O diffusion, hence significant resorption, occurred even on rapid quench timescales (samples were estimated to have cooled from the experimental temperature of 825°C through the glass transition in less than 5 s). However, the low melt H_2O_t content inferred from the low OH contents of the Od-1 tephra would both reduce H_2O_t diffusivity by two orders of magnitude and increase T_g compared to the experimental study, and the tephra would therefore be less susceptible to significant modification of H_2O speciation through quench resorption.

Syn-eruptive hydration by external water was documented for pumice pyroclasts from the 2012 eruption of Havre volcano in the Kermadec arc (Mitchell et al., 2018; Mitchell et al., 2022). FTIR H_2O species data revealed disequilibrium speciation with

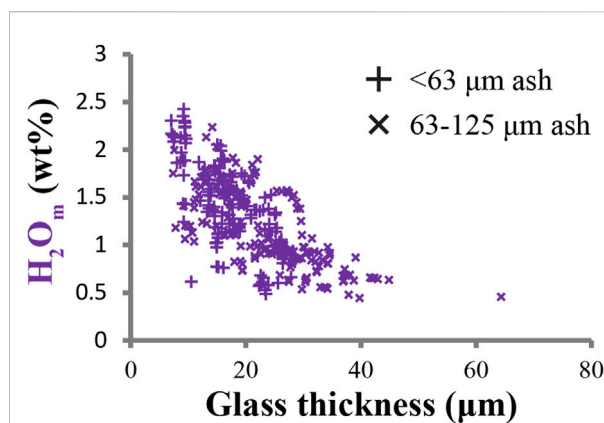


FIGURE 6
FTIR H_2O_m data for all individual spectra from the <63 µm and 63–125 µm size fractions. The general trend of higher H_2O_m wt% for thinner glasses is evidence for hydration of tephra by external water.

excess H_2O_m that could not be explained by slow low temperature hydration by seawater in the short time since eruption. Low OH contents indicated that pumice had degassed to low pressures near the sea surface. Mitchell et al. (2018) therefore concluded that the excess H_2O_m indicated syn-eruptive hydration by condensed magmatic vapor and entrained seawater occurring on timescales of minutes as the buoyant clasts ascended in a submarine plume above the deep vent, a mechanism that is consistent with numerical modelling of cooling rates and ascent speeds of the Havre pumice (Manga et al., 2018) and subsequent isotope analysis (Mitchell et al., 2022). The slow cooling of these pumice was possible because of their size (up to several meters in the case of the Giant Pumice deposit) and their presumed insulation within a warm submarine plume. Smaller particles like ash grains would be expected to cool much more rapidly and thus have less opportunity for syn-eruptive hydration than large pumice clasts. However, some syn-eruptive hydration of ash by external water was recently documented by Hudak et al. (2021) for ash from the subaerial 2009 phreatomagmatic eruption of Redoubt volcano in Alaska, United States. Bulk H_2O_t and hydrogen isotopic measurements revealed that some ash had gained up to 0.4 wt% H_2O_t by hydration, and diffusion modelling led to the conclusion that this happened during cooling over the range 500°C–100°C in an eruption plume containing vaporized glacial meltwater. Although no measurements of H_2O speciation were made, it can be assumed that at these temperatures and timescales the water added by hydration as H_2O_m would have little to no time for interconversion to OH, producing similar disequilibrium speciation to the other hydration scenarios. Diffusion modelling and observations of tephra characteristics indicated that the hydration at Redoubt was likely restricted to ash at the margins of the plume where interaction with vaporized

meltwater could occur while ash particles were still at relatively high temperature ($>400^{\circ}\text{C}$), whereas ash that was insulated within the drier plume interior only encountered entrained meltwater after cooling to temperatures at which significant hydration could no longer occur (Hudak et al., 2021). Although a submarine eruption of Oomurodashii can be expected to have similar conditions of abundant external water at plume margins, the relative impact of syn-eruptive hydration on the Od-1 tephra is expected to be less significant due to differing glass thickness. In Redoubt tephra, glasses (bubble walls and glass selvages on crystals) are only 1–3 μm thick, such that the ~ 1 μm diffusion profiles resulting from syn-eruptive hydration can significantly increase their bulk H_2O_t content. By contrast, the average thickness of the <63 and 63–125 μm grains analyzed in the Od-1 tephra is 21 μm (Table 1). Any contribution to the measured H_2O contents by syn-eruptive hydration is therefore likely negligible or minor at most (see also Figure 2 in Hudak et al., 2021).

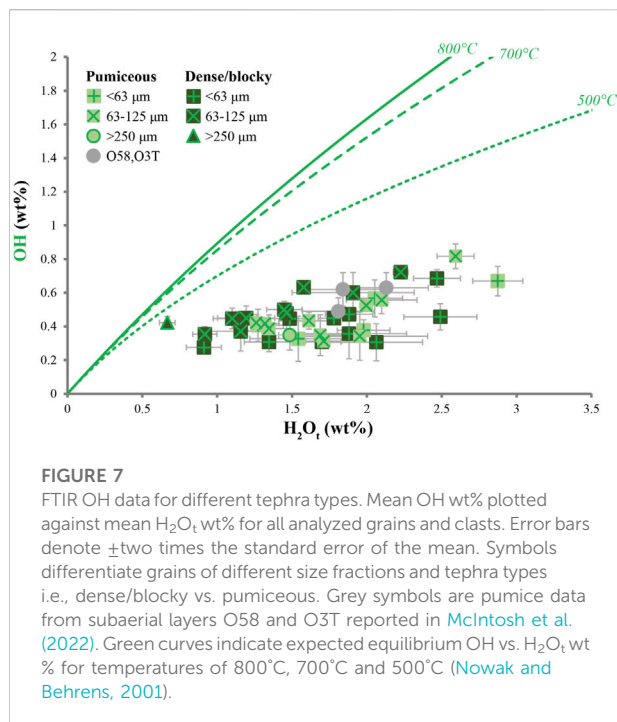
Instead, the observed disequilibrium speciation is most likely explained by *secondary hydration*, i.e., the slow low temperature addition of water from the surrounding environment in the time since eruption and deposition (Friedman and Smith, 1958). Secondary hydration has been shown to be widespread and to have altered the water contents of many volcanic glasses, in both subaerial and submarine deposits, with high silica glasses like rhyolite and vesicular glasses with interconnected porosity and high surface areas being particularly susceptible (e.g., Bryant et al., 2003; Helo et al., 2011; Giachetti and Gonnermann, 2013; Kutterolf et al., 2014; Dingwell et al., 2016; Seligman et al., 2016; Ikehara et al., 2017). During hydration, water enters the glass as H_2O_m , the diffusing H_2O species, and remains as H_2O_m because the species interconversion reaction is negligible at low temperature (McIntosh et al., 2017). The H_2O_m content, hence H_2O_t content, of the glass therefore increases but the OH content remains the same as when it crossed the glass transition after eruption (Figure 1).

Evidence for external hydration as the cause of the disequilibrium speciation of the Od-1 tephra is seen in the relationship between glass thickness and H_2O_m content (Figure 6). A plot of glass thickness vs. H_2O_m concentration for all individual spectra measurements for grains in the <63 and 63–125 μm size fractions shows that H_2O_m wt% is generally higher for thinner glasses, which would be relatively more affected by addition of H_2O_m at their surfaces than thicker glasses. Glass thickness is only a proxy for the overall surface area of a grain, which will also be determined by its shape and amount of interconnected porosity, and this is reflected in the scatter of the data. Further evidence for external hydration is that the mean H_2O_m :OH ratio (also reflected in the ϵ_{3500} value, Table 1) of smaller <63 μm grains (3.4) is higher than for 63–125 μm grains (2.5), and that for the larger grains and clasts the ratio is higher for pumiceous grains with higher

surface area than for dense blocky grains. Thus, the thick, low porosity >250 μm dense clast has the lowest H_2O_m content of all samples and its speciation lies closest to expected equilibrium temperature curves, although even this sample has experienced enough hydration to produce disequilibrium speciation (Figure 5).

4.2 Hydration modelling of submarine tephra

The array of glass thickness and FTIR H_2O data for the Od-1 tephra, in addition to the constrained eruption age of 13.5 ka, enables us to further validate the assumption of slow low temperature secondary hydration *via* numerical modelling of H_2O diffusion. Each set of glass thickness and FTIR wt% data is treated as relating to a glass slab of that thickness undergoing hydration from both surfaces for a total of 13.5 kyr, which results in the measured FTIR H_2O contents. We assume that the source of the external water is seawater trapped in the pore space within the seafloor sedimentary column, which will always maintain a fixed concentration boundary condition at the glass surface. We use a constant temperature of 4°C to reflect the stable, cold environment of seafloor sediments and a constant pressure of 20 MPa to reflect the current hydrostatic pressure at the seafloor at the depth of the drill site ($\sim 2,000$ m b.s.l.). Although the ambient pressure of the Od-1 tephra would change over time due to changes in sea level and burial depth, the pressure dependence of H_2O diffusivity is negligible over the expected range (e.g., Ni and Zhang, 2008). H_2O solubility in glass at Earth surface temperatures and pressures is not well constrained and must be assumed. Based on studies reporting bulk H_2O_t contents of up to 4 wt% in unaltered hydrated obsidians (Denton et al., 2009; Denton et al., 2012) and up to 5 wt% in unaltered hydrated pumice and tephra deposits (Denton et al., 2009; Giachetti and Gonnermann, 2013; Seligman et al., 2016), we compare results for boundary conditions of 4 wt% and 5 wt%. The initial H_2O_t content of the glass is set equal to the measured OH wt%, assumed to be unaltered by low temperature secondary hydration, because for the low OH contents of the Od-1 tephra little or no coexisting H_2O_m would be expected at magmatic temperatures. The initial H_2O_m content of the glass is therefore set to 0 wt%. Although H_2O diffusivity ($D_{\text{H}_2\text{O}}$) is known to depend on the concentration of H_2O_t at $>400^{\circ}\text{C}$ (e.g., Zhang and Behrens, 2000; Ni and Zhang, 2008), and studies have shown this concentration dependence likely continues at low temperature (e.g., Seligman et al., 2016; Hudak and Bindeman, 2020), studies of low temperature hydration often report constant “apparent” or “characteristic” values of $D_{\text{H}_2\text{O}}$ (e.g., Giachetti and Gonnermann, 2013, and references therein). We therefore compare two versions of the hydration model: one where $D_{\text{H}_2\text{O}}$ is assumed to be constant, and one where $D_{\text{H}_2\text{O}}$ varies as concentration increases during hydration. For the

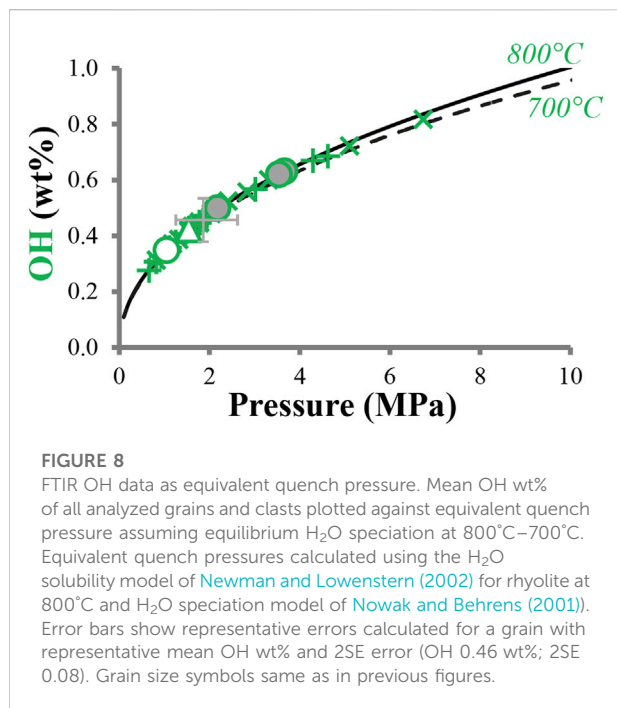


concentration-dependent DH_2O model we follow the approach of Seligman et al. (2016) and Hudak et al. (2021) of extrapolating the functional form of the Zhang and Behrens (2000) diffusivity formulation, derived from experimental data $>400^\circ\text{C}$, to low temperatures, which requires determining a constant prefactor value to scale it to fit low temperature data. Whereas those studies used bulk H_2O_t measurements, our data consist of H_2O species data measured by FTIR. We therefore elect to model the diffusivity of H_2O_m (DH_2O_m) rather than diffusivity of H_2O_t (DH_2O_t), but extrapolate the Zhang and Behrens (2000) formulation for DH_2O_m to low temperature in the same way i.e., by determining a suitable constant prefactor from our data.

We begin by focusing on the data from the $<63\ \mu\text{m}$ size fraction, because these smaller grains will be least affected by differences in surface area between the ‘dense’ and ‘pumiceous’ types. For each shard thickness and measured H_2O_m wt%, we can find the apparent diffusivity (when assuming a constant diffusivity) or prefactor (when assuming a concentration-dependent diffusivity) that would result in the same level of hydration within the known age of the sample, 13.5 ka. This effective “reverse engineering” of relevant parameters is achieved using a simple, iterative bisection method, commonly used to find the roots of continuous, monotonically varying functions. Details are given in the Supplementary Material. For these data, the constant DH_2O_m hydration model yields an apparent diffusivity of $\sim 1.62 \times 10^{-23}\ \text{m}^2/\text{s}$ assuming a boundary condition of 4 wt%. This falls within the full range of characteristic diffusivities reported from obsidian hydration dating ($0.1\text{--}127 \times 10^{-23}\ \text{m}^2/\text{s}$; summarized in Giachetti and

Gonnermann (2013) and is consistent with characteristic diffusivities determined for secondary hydration of subaerial volcanic pyroclasts ($\sim 10^{-23}\ \text{m}^2/\text{s}$; (Giachetti and Gonnermann, 2013). For the concentration-dependent hydration model, we use the $<63\ \mu\text{m}$ size fraction data to calculate the necessary constant prefactor value for the low temperature extrapolation of the Zhang and Behrens (2000) DH_2O_m equation. Using a 4 wt% boundary condition, the resulting prefactor values have a mean value of 5.87 with a standard deviation of 2.73. This corresponds to DH_2O_m of $1.99 \times 10^{-26}\ \text{m}^2/\text{s}$ at 0.1 wt% H_2O_t and $3.38 \times 10^{-23}\ \text{m}^2/\text{s}$ at 4 wt% H_2O_t . There is little difference in calculated diffusivity values with a boundary condition of 5 wt% H_2O_t , which yields $\sim 1.04 \times 10^{-23}\ \text{m}^2/\text{s}$ assuming a constant diffusivity or a prefactor of 0.69 for concentration-dependent diffusivity. The good agreement of these calculated diffusivity values with those published for secondary hydration of subaerial glasses is further supporting evidence for our assumption that the disequilibrium speciation of the Od-1 tephra is caused by low temperature secondary hydration after eruption.

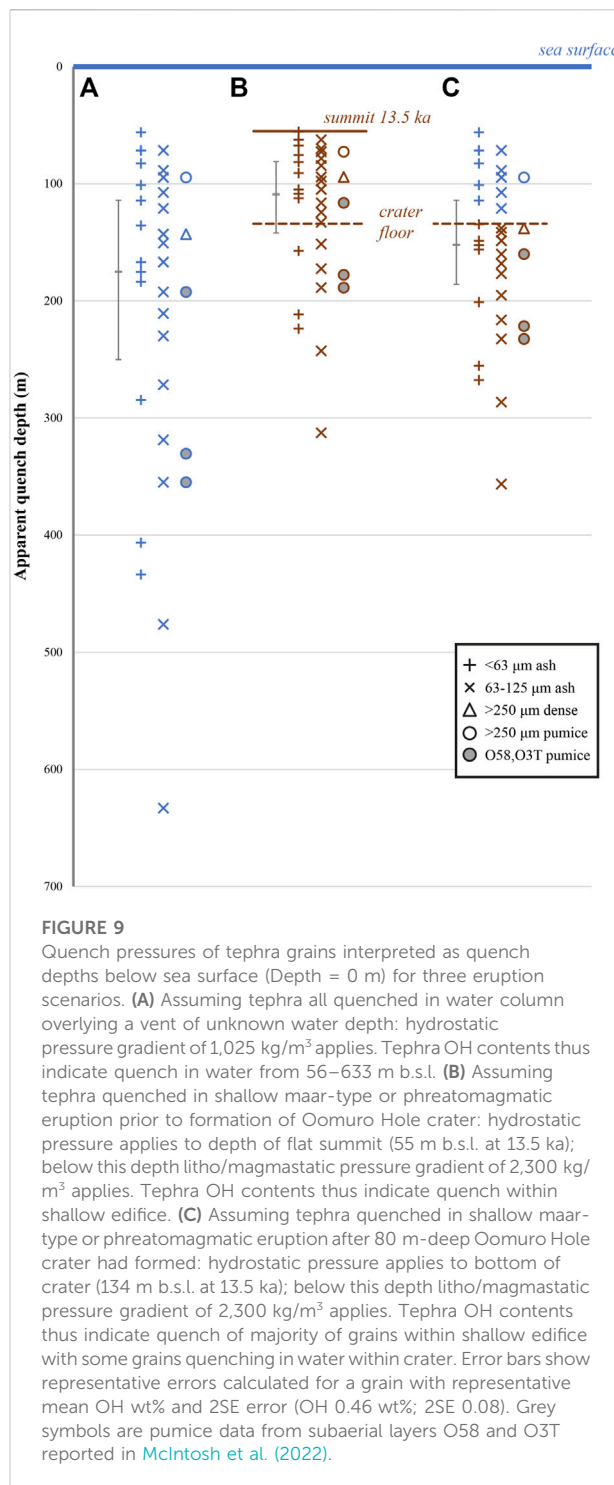
We then investigated the possibility that similar numerical modelling of low temperature hydration could be used to estimate the ages of hydrated tephra. Taking the diffusivity and prefactor values constrained from the $<63\ \mu\text{m}$ size fraction, we then treated the 63–125 μm size fraction as tephra of ‘unknown’ age, and used the hydration model to estimate their age from their glass thickness and FTIR H_2O data. Calculated ages are relatively insensitive to the choice of wt% at the boundary, and yield $\sim 16.8\ \text{ka}$ (standard error of the mean: ~ 685 years) and $\sim 15.0\ \text{ka}$ (standard error of the mean: ~ 480 years) for constant diffusivity and concentration-dependent diffusivity, respectively. That these ages are close to the known age of 13.5 ka demonstrates the validity of both diffusivity approaches for modelling low temperature hydration of tephra, although it is possible that accounting for concentration-dependent diffusivity will be increasingly important for thinner or younger glasses due to the increased relative importance of the shape of the calculated hydration profile. Both approaches are likely to slightly overestimate tephra ages due to the simple 1D model, which neglects any addition of H_2O_m from other surfaces; however, this preliminary study indicates the likely magnitude of this resulting uncertainty. In future, this FTIR-and-hydration modelling method for estimating tephra ages can be further refined by testing on diverse tephra datasets. For example, is there a maximum age for successful dating beyond which the full thickness of the tephra shard becomes completely hydrated? How may hydration conditions be affected for tephra in deep sediments with significant compaction and reduction in pore space, or where pore fluid chemistry and pH differ significantly from seawater? And can the hydration model be further improved by accounting for the 3D morphology of tephra grains, in which hydration may proceed from all surfaces? In this initial study we suggest that the diffusivity values derived here may be applicable



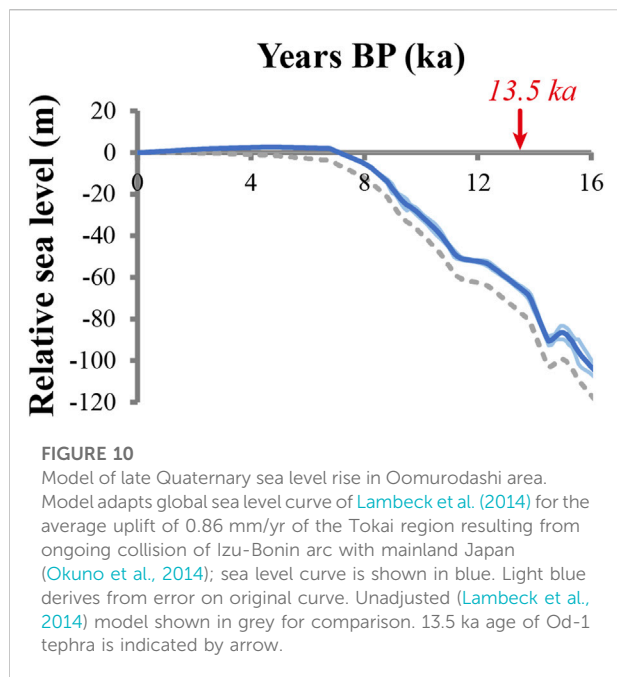
to other tephra in marine sedimentary cores experiencing hydration under similar conditions, and which have not been affected by subsequent reheating of the deposit. Hydration modelling of FTIR H₂O data may offer a valuable additional method for constraining eruption ages of such tephra, particularly for cores located beneath the carbonate compensation depth (CCD) where calcite shells of marine organisms used for ¹⁴C or ¹⁸O dating methods are not preserved. For the purposes of this study's investigation of Oomurodashi, however, we take our low temperature hydration modelling results as further supporting evidence that the disequilibrium H₂O speciation of the Od-1 tephra is caused by secondary hydration, a process that does not alter OH contents from when the magma was originally quenched to glass. As in McIntosh et al. (2022), we therefore use these OH contents for our subsequent investigation of the eruption processes that created this tephra deposit.

4.3 Comparison of shard types and size fractions

Figure 7 shows the mean OH vs. H₂O_t contents for each shard and clast categorized by size fraction and tephra type i.e., dense and blocky or pumiceous. Data for the different size fractions lie within the same range and there is no evidence for different OH values depending on tephra type. This is supported by the results of two sample t-tests that found there was no difference in mean OH wt% between the <63 μm size fraction (mean = 0.43 wt%, σ = 0.13) and the 63–125 μm size fraction



(mean = 0.48 wt%, σ = 0.14; $t(32) = -1.14$, $p = 0.26$), or between the dense tephra type (mean = 0.45 wt%, σ = 0.13) and the pumiceous tephra type (mean = 0.45 wt%, σ = 0.14; $t(34) = -0.03$, $p = 0.98$). All tephra therefore appears to have undergone similar degassing histories, regardless of size or physical characteristics such as vesicularity.



4.4 Interpreting OH contents as quench pressures

OH contents, locked in as the sample cooled through the glass transition, can be used to estimate the pressure at which the hydrated tephra grains were quenched by choosing appropriate models of H_2O solubility and speciation and applying likely T_g ($= T_{ae}$) values. Strictly speaking, T_g refers to glass transition temperature as measured under a specific set of experimental conditions, but for simplicity we are going to use T_g in the following discussion to mean “a feasible temperature for the glass transition (based on consideration of the sample’s likely initial H_2O_t content and cooling history) at which H_2O species interconversion ceased and the amount of OH became fixed”. As discussed in Section 4.1, we consider T_g of 800–700°C to be a reasonable assumption for the Od-1 tephra.

We use the VolatileCalc H_2O_t solubility model for rhyolite at 800°C to output how H_2O_t solubility varies with pressure (Newman and Lowenstern, 2002). We assume a pure- H_2O_t system with no CO_2 , on the basis that no dissolved CO_2 was detected (minimum detection limits ~7 ppm), that CO_2 content is not expected to be high based on melt inclusions of other rhyolite magmas in the Izu-Bonin (e.g., Allen et al., 2010), and that the low OH contents of the tephra indicate they had degassed to low pressures by which point any CO_2 would be expected to have exsolved and outgassed through connected porosity (e.g., Lowenstern, 2001). For every H_2O_t value output by the VolatileCalc solubility model we calculate the equivalent OH contents at a specified T_g via the H_2O speciation model for rhyolite of Nowak and Behrens (2001). Note that the H_2O species

data automatically output by the VolatileCalc model were not used, because they do not account for temperature dependence of H_2O speciation (i.e., in a graph of OH or H_2O_m vs. H_2O_t , H_2O species data output by VolatileCalc’s Rhyolite H_2O Solubility vs. Pressure calculation will all plot on the same curves regardless of calculation temperature). It can be seen that the exact choice of T_g value makes little difference to estimated pressures for the Od-1 tephra because T_g lines (T_{ae} lines) converge at low H_2O_t and pressure (Figures 7, 8).

The resulting estimated quench pressures of Od-1 tephra grains and clasts are shown in Figure 8. No grains degassed to atmospheric pressure, at which a saturated rhyolite melt would be expected to contain ~0.1 wt% OH. Instead, estimated quench pressures range from ~0.7–7.1 MPa, with the interquartile range falling between 1.1 and 2.4 MPa.

4.5 Interpreting estimated quench pressures as quench depths

Quench pressures can be interpreted as quench depths by applying an appropriate depth-pressure gradient. As T_g choice makes negligible difference to the estimated quench pressures, for this we use pressures calculated assuming $T_g = 800^\circ C$. We consider three eruption scenarios (Figure 9). In the first scenario, we assume that the Od-1 tephra quenched in a submarine plume erupted from a vent at an unknown water depth. Quench pressures are therefore converted to equivalent depths below sea level assuming a hydrostatic pressure gradient with seawater density of 1,025 kg/m³. Doing so gives a quench depth range of 56–633 m b.s.l., with the interquartile range lying between 94 and 216 m b.s.l. (Figure 9A). To consider how these apparent quench depths compare to the water depth of the Oomurodashii edifice at the time of eruption, we use a region-specific model of past sea level rise that accounts for both global change in ice equivalent volume and local tectonic processes affecting relative sea level (McIntosh et al., 2022) (Figure 10). This sea level curve adapts the global sea level curve of Lambeck et al. (2014) for the average uplift of 0.86 mm/yr calculated for the Tokai region as a result of the active collision of the Izu-Bonin arc with mainland Japan (Okuno et al., 2014). This sea level curve successfully reproduces the magnitude and timing of the late Holocene high stand observed in the region (Fujii and Fuji, 1967; Umitsu, 1991) and gives a low stand of ~120 m below current sea level at the time of the Last Glacial Maximum, which corresponds to the current depth of the flat Oomurodashii summit that is thought to have been produced by wave planation at that time.

The hydrostatic pressure gradient is only applicable between the sea surface and the eruptive vent. According to the region-specific model of past sea level, at 13.5 ka the flat summit of Oomurodashii would have been 55 m b.s.l. (i.e., sea level was 65 m lower than today). This is roughly equal to the shallowest apparent quench depth of 56 m b.s.l.; however, a deeper

eruptive vent would be necessary to explain the rest of the data if all the tephra quenched in water. The floor of the Oomuro Hole crater today is ~80 m below the flat summit; if the same size crater existed when the Od-1 tephra was erupted its floor would be 134 m b.s.l., which is still too shallow to explain 60% of the apparent tephra quench depths. The presence of a lava knoll elsewhere on the flat summit with estimated eruption age ~7–10 ka indicates that not all of Oomurodashi's late Quaternary eruptions have been confined to the Oomuro Hole crater (McIntosh et al., 2022). However, ROV surveys and bathymetry (Figure 2) did not identify any other potential eruptive vents, particularly not in water depths great enough to explain the apparent quench depths of the majority of the tephra. Instead, we conclude that a purely hydrostatic gradient cannot explain the observed volatile contents of the Od-1 tephra.

In the second and third quench depth scenarios we therefore consider a hybrid hydro-litho/magmatic pressure gradient. Hydrostatic pressure applies until the water depth of the vent, after which a lithostatic or magmatic pressure gradient applies within the shallow edifice or upper magma conduit. McIntosh et al. (2022) proposed that the subaerial O58 and O3T deposits on Izu-Oshima and Toshima islands were formed by a shallow phreatomagmatic eruption that created the Oomuro Hole crater within the flat summit, and based on the geochemical and stratigraphic correlation of the deposits we consider the possibility that the Od-1 tephra results from the same crater-forming eruption. In the second scenario (Figure 9B) we therefore consider the case where the crater has not yet formed (i.e., the litho/magmatic gradient applies from the depth of the flat summit at 55 m b.s.l.), while in the third scenario (Figure 9C) we consider the case where a crater of 80 m depth had already formed (i.e., the litho/magmatic gradient applies from 134 m b.s.l.). For the portion within the upper edifice/conduit we use a density of 2,300 kg/m³ to approximate either a conduit filled with vesicular magma, a coherent edifice constructed of similarly vesicular volcanic products, or a maar-type vent filled with unconsolidated volcanoclastic debris.

Applying the second scenario, the tephra quench pressures would indicate that all Od-1 grains quenched within the shallow Oomurodashi edifice, rather than in the overlying water column (Figure 9B). Three-quarters of the grains would have quenched in the upper 80 m of the edifice, i.e., within the depth of the crater observed today. Applying the third scenario, in which the crater already existed, ~40% of grains would quench in the water column within the crater and the rest in the shallow conduit within ~200 m of the crater floor (Figure 9C).

4.6 Consideration of disequilibrium degassing

The above calculations assume the case of equilibrium degassing, in which the rate of H₂O diffusion into bubbles in

response to decompression as magma ascends is sufficiently fast to maintain melt H₂O_t contents in equilibrium with the ambient pressure. If instead disequilibrium degassing conditions applied, the melt would become oversaturated with H₂O_t with respect to the ambient pressure so the actual quench pressure, hence depth, would be shallower than calculated. Disequilibrium degassing may occur when inter-bubble distances are too large to enable efficient degassing and/or when magma ascent is particularly rapid (e.g., Sparks, 1978; Mangan et al., 2004; Gonnermann and Manga, 2007). The vesicular pumiceous Od-1 tephra type would not be affected by degassing limited by inter-bubble distances. The denser tephra type is less vesicular than the pumiceous type but does still contain bubbles (Figure 4), and the fact that the OH contents of both tephra types overlap (Figure 7) therefore suggests that volatile exsolution was not limited by inter-bubble spacing. Magma ascent rate for the eruption is unknown, but there is no reason to assume that it was particularly rapid. The proposed mechanism of a phreatomagmatic eruption (McIntosh et al., 2022) may in fact be favored by slow to moderate magma ascent rates compatible with equilibrium degassing conditions, because these ascent rates provide better opportunities for the necessary magma-water interaction (Aravena et al., 2018).

The degree to which disequilibrium degassing and related volatile oversaturation may occur during eruptions is a significant topic of research. Disequilibrium degassing processes have been replicated in laboratory experiments, but these typically emulate conditions at high pressure in the deep conduit where bubble nucleation conditions can be a controlling factor (e.g., Mangan et al., 2004). At lower pressures, these experiments tend to show that increasingly rapid decompression rates are required to maintain volatile oversaturation and disequilibrium degassing processes (e.g., Burgisser and Gardner, 2004). Literature data for matrix glass volatile contents of pyroclastic deposits are sparse, in large part because secondary hydration alters the bulk H₂O_t content of such samples (Giachetti and Gonnermann, 2013). Although numerical modelling of conduit processes has suggested that explosive eruptions may exhibit disequilibrium degassing and volatile oversaturation of as much as 1 wt% at the point of melt fragmentation (e.g., Proussevitch and Sahagian, 2005), studies of explosive eruption deposits that have been able to exclude effects of secondary hydration suggest that many pyroclasts appear to have degassed most of their magmatic volatiles prior to quench. For example, unhydrated pumice from the climactic phase of the 1991 CE Pinatubo eruption had 0.3 wt% H₂O_t (Gerlach et al., 1996), and the 2011–12 eruption of Cordon Caulle, Chile, produced pumice with 0.1–0.3 wt% H₂O_t during its Plinian phase (Castro et al., 2014) and pumiceous ash with 0.14 wt% H₂O_t during subsequent ash jetting and Vulcanian activity (Schipper et al., 2013). Meanwhile, the 'driest' (i.e., least affected by syn-eruptive hydration) tephra from the 2009 Redoubt eruption had 0.46 wt% H₂O_t (Hudak et al.,

2021), and pumice from the 1060 CE eruption of Glass Mountain, California, appears to have contained ~0.2–0.5 wt% H₂O_t upon eruption after correcting for the effects of secondary hydration (Giachetti et al., 2020, 2015). Excitingly, the new application of imaging FTIR for thin and/or vesicular glasses, combined with the species-dependent ϵ_{3500} method necessary for analyzing hydrated glasses, now makes it easier to assess the magmatic volatile contents of matrix glasses, without the need to correct bulk H₂O_t measurements for crystal contents (e.g., Hudak et al., 2021) or assume sample porosity and diffusivity parameters in hydration modelling (e.g., Giachetti et al., 2015; Seligman et al., 2016). This will assist in comprehensive assessment of the likely degree of volatile oversaturation and/or pressures of fragmentation and quench for pyroclasts from a wide range of eruption styles and intensities. For now, we can say that for the Od-1 tephra there is no reason to assume disequilibrium degassing conditions and that the volatile data are consistent with fragmentation and quench within the shallow edifice, with the additional possibility that some quenched within the water column during or after formation of a shallow crater like Oomuro Hole.

4.7 Implications for eruption style

The combination of tephra characteristics and volatile contents and their similarities with those of the O58 and O3T subaerial tephtras support the interpretation that the Od-1 tephra records the same phreatomagmatic eruption that formed the Oomuro Hole crater. The pumiceous tephra type may record primary degassing and magma shearing processes within the conduit during ascent, yet the relatively low vesicularity of the dense blocky tephra type indicates that bubble overpressure-driven fragmentation of magma did not dominate. Instead, their blocky shapes and frequent occurrence of brittle step-like fractures on outer surfaces (Figure 4) are key characteristics of brittle quench fragmentation indicative of magma-water interaction (e.g., Büttner et al., 1999; Büttner et al., 2002; Dellino et al., 2012; Fuller et al., 2018). Such particles were also observed in the subaerial tephtras (McIntosh et al., 2022). The subaerial tephtras also contained particles that were aggregates of very fine ash grains, which are also potentially indicative of phreatomagmatic processes. Such particle aggregates were not found in the Od-1 tephra; however, this is not unexpected since ash aggregates will rapidly disintegrate when dropped in water and are almost never found in deep sea tephra (Freundt et al., 2021).

The OH contents of the Od-1 tephra have been shown to be consistent with quench fragmentation within the shallow volcanic edifice at depths related to formation of the Oomuro Hole crater, possibly transitioning into some grains quenching within the water-filled crater as it formed. As in McIntosh et al. (2022), we consider whether this phreatomagmatic eruption was

the result of maar-type explosions within a partly infilled vent, or of a more sustained eruption style incorporating shallow magma-water interaction in a magma-filled conduit. The morphology of the Oomuro Hole crater, which is excavated into Oomurodashi's flat summit without any significant accumulation of pyroclastic material around the rim to form a pyroclastic cone feature (Figure 2), is consistent with typical maar crater morphology (e.g., White and Ross, 2011; Palladino et al., 2015). Although maar-type and diatreme phreatomagmatic explosions can occur at a large range of conduit depths, the relatively shallow quench depths interpreted for both the subaerial and submarine tephra deposits are consistent with the shallow depths necessary for such explosions to produce surface ejection of tephra (e.g., Graettinger et al., 2014; Sweeney and Valentine, 2015). Another consideration is that maar-type eruptions typically produce lithic-rich deposits (e.g., White and Ross, 2011). The subaerial O58 deposit on Izu-Oshima contains cm-size angular lava fragments at its base interpreted to derive from the excavation of the Oomuro Hole crater, which ROV surveys show cross-cuts at least one vesicular rhyolite lava (McIntosh et al., 2022). These volcanic lithics highlight that it can be difficult to distinguish juvenile and lithic material for phreatomagmatic explosions occurring in shallow volcanic edifices (e.g., White and Houghton, 2006). It is possible that some of the rarer tephra types in the Od-1 deposit, such as microlite-rich grains or grains with small but distorted, possibly collapsing bubbles (Figure 4), may in fact be lithics derived from fragmentation of previously erupted material comprising the shallow edifice. However, lithics were only confirmed at the base of the O58 deposit, rather than occurring repeatedly throughout the layer as might be expected if it resulted from repeated, discrete explosions excavating the Oomuro Hole crater. Moreover, maar-type eruptions typically do not create widely-dispersed deposits. For example, the 1977 Ukinrek Maars eruption in Alaska dispersed fine ash to 160 km but significant tephra accumulation was restricted to within 3 km of the vent (Kienle et al., 1980; Self et al., 1980); similarly, the deposits of the ~1 ka BP eruption of Nejapa Maar in Nicaragua thin to 1 m thickness within 3 km of the vent (Rausch and Schmincke, 2010). The O58 and O3T tephtras already indicated fallout at ~15–20 km from Oomuro Hole, which the Od-1 tephra now extends to ~45 km. Submarine tephra deposits can be formed or remobilized by density currents moving down the submarine edifice (e.g., Kano et al., 1996; Freundt et al., 2021), but the presence of a submarine canyon between Oomurodashi and the C9010E drillsite suggests that the Od-1 tephra instead records fallout from a subaerial plume. Accordingly, we suggest that the 13.5 ka eruption is more likely to have been, or to have transitioned to, a phreatomagmatic eruption involving magma-water interaction in the shallow conduit that was powerful enough to create a sustained subaerial plume, akin to the 2010 “pulsating” eruption of Eyjafjallajökull, Iceland (Dellino et al., 2012; Dürig et al., 2015). The C9010E core is ultimately only one point from within the full dispersal area of the submarine

tephra deposit. It is hoped that future drilling and coring of marine sediments in the northern Izu-Bonin may recover more samples of this and potentially other Oomurodashi eruption deposits, enabling detailed assessment of eruption magnitude and processes of tephra transport and deposition.

Such information is also important for assessing likely hazards of future eruptions of Oomurodashi. Due to Holocene sea level rise, the Oomuro Hole crater is now 65 m deeper than at the time of the 13.5 ka eruption (Figure 10). Despite this slightly increased hydrostatic pressure at the vent, it is likely that a similar magnitude phreatomagmatic eruption from the Oomuro Hole crater could create surface hazards including subaerial fallout, explosive blasts, and potentially related tsunami activity such as those observed during the 1952-3 Myojin-sho eruption (Morimoto and Osaka, 1955; Fiske et al., 1998) and recent 2022 Hunga Tonga—Hunga Ha'apai eruption. Submarine pumice deposits observed during ROV surveys (Tani et al., 2013; McIntosh et al., 2022) raise the possibility of larger magnitude eruptions as well. A major question remains whether Oomurodashi has produced pumice rafts such as those from the 1924 Iriomote (Kazuo Seki, 1927) and 1986 and 2021 Fukutoku-Oka-no-Ba eruptions (Kato, 1988; Oikawa, 2021) and, if so, whether it may produce them again in the future. Floating pumice rafts may ultimately be dispersed several thousand kilometers from their source vents before sinking or being stranded along coastlines (e.g., Frick and Kent, 1984; Bryan et al., 2012). It is an active topic of research to determine if evidence of pumice rafts is preserved and identifiable within the local marine geological record. As well as efforts to geochemically fingerprint stranded pumice in coastal deposits (e.g., Bryan, 1971; Shiraishi et al., 1992; Ward and Little, 2000), it may be important to also target isolated pumice clasts in marine sediment cores that may represent 'drop stones' from widely dispersed pumice rafts (e.g., Pattan et al., 2008). Through increasingly sophisticated comparisons of geochemical data using expanding tephra databases, innovative statistics and machine learning approaches (e.g., Iwamori et al., 2017; Bolton et al., 2020), such innocuous isolated pumice clasts may be key to identifying pumice raft-forming events at volcanoes far from the location of the marine sedimentary core itself, while FTIR volatile analysis of their matrix glasses will provide insights into the degassing and eruption processes related to their formation.

5 Conclusion

The matrix glass volatile contents and physical characteristics of the Od-1 tephra layer in the C9010E marine sediment core

support the interpretation that it was produced by the same 13.5 ka shallow phreatomagmatic eruption that formed the Oomuro Hole crater and produced the subaerial O58 and O3T tephra layers on Izu-Oshima and Toshima islands. Although all tephra grains were affected by low temperature secondary hydration and alteration of original magmatic H₂O contents, with the extent of hydration controlled by grain size and porosity characteristics, we show that OH contents can be successfully quantified by imaging FTIR analysis and used to interpret degassing and eruption processes of hydrated volcanic glasses. FTIR data also show potential for use as a method of estimating eruption ages of marine tephra, *via* numerical modelling of low temperature hydration. FTIR volatile data therefore offer a new way of identifying and correlating marine tephra deposits and investigating the eruption processes that generated them. Moreover, the increasing application of imaging FTIR volatile analysis to vesicular lavas, pyroclasts, and tephra will enable comprehensive assessment of issues related to shallow conduit degassing processes for different eruption conditions, such as depths of quench fragmentation or degree of disequilibrium degassing-induced volatile oversaturation, that will improve our understanding of eruption processes for both submarine and subaerial volcanoes.

Data availability statement

The original contributions presented in the study are included in the article/Supplementary Material, further inquiries can be directed to the corresponding author.

Author contributions

IM conceived the project, undertook FTIR measurements and data analysis, and led the writing of the manuscript. KA led chemical analysis of tephra and interpretation of tephrostratigraphy. MK, MM and TS assisted with sampling of C9010E core tephra and subaerial tephra on Izu-Oshima and with integration of tephrostratigraphy datasets. TY modified and translated the numerical modelling code of Hudak and analysed the FTIR data using the diffusion model. All authors discussed the results and contributed to the final manuscript.

Funding

This research was supported by Japan Society for the Promotion of Science KAKENHI grant number JP00470120.

Acknowledgments

We thank Michael Hudak for kindly sharing and discussing his numerical modelling code. We thank the crew and shipboard scientific party of the *D/V Chikyu* and cruises NT12-19 of *R/V Natsushima* and KS-16-6 of *R/V Shinseimaru*. We thank C. Helo and C. Allison for their thoughtful comments, which helped to improve our manuscript.

Conflict of interest

The authors declare that the research was conducted in the absence of any commercial or financial relationships that could be construed as a potential conflict of interest.

References

- Allen, S. R., Fiske, R. S., and Tamura, Y. (2010). Effects of water depth on pumice formation in submarine domes at Sumisu, Izu-Bonin arc, Western Pacific. *Geology* 38, 391–394. doi:10.1130/G30500.1
- Aoki, K., Kobayashi, M., Murata, M., and Suzuki, T. (2019). “Tephrostratigraphy of drilled core C9010E off the Boso peninsula: As a preliminary report,” in *JpGU meeting 2019: Abstract HQR05-05* (Chiba: Japan Geoscience Union).
- Aoki, K., Kobayashi, M., Murata, M., Nishizawa, T., Takahashi, T., and Suzuki, T. (2020). “Construction of late quaternary eruption history in and around the Izu volcanic islands, off Tokyo,” in *Ocean sciences meeting 2020: Abstract mg14a-2178* (San Francisco: American Geophysical Union).
- Aoki, K. (2008). Revised age and distribution of ca. 87 ka Aso-4 tephra based on new evidence from the northwest Pacific Ocean. *Quat. Int.* 178, 100–118. doi:10.1016/j.quaint.2007.02.005
- Aoki, K. (2020). Dawson tephra, a widespread 29-ka marker bed, in a marine core from Patton Seamount off the Alaska Peninsula and its potential marine-terrestrial correlation. *J. Quat. Sci.* 35, 93–101. doi:10.1002/jqs.3176
- Aravena, A., de' Michieli Vitturi, M., Cioni, R., and Neri, A. (2018). Physical constraints for effective magma-water interaction along volcanic conduits during silicic explosive eruptions: Reply. *Geology* 47, e462–e870. doi:10.1130/G46200Y.1
- Behrens, H., Tamic, N., and Holtz, F. (2004). Determination of the molar absorption coefficient for the infrared absorption band of CO₂ in rhyolitic glasses. *Am. Mineralogist* 89, 301–306. doi:10.2138/am-2004-2-307
- Bolton, M. S. M., Jensen, B. J. L., Wallace, K., Praet, N., Fortin, D., Kaufman, D., et al. (2020). Machine learning classifiers for attributing tephra to source volcanoes: An evaluation of methods for Alaska tephra. *J. Quat. Sci.* 35, 81–92. doi:10.1002/jqs.3170
- Bronk Ramsey, C. (2005). *OxCal v. 3.10*.
- Bronk Ramsey, C. (2021). *OxCal v. 4.4*.
- Bryan, S. E., Cook, A. G., Evans, J. P., Hebden, K., Hurrey, L., Colls, P., et al. (2012). Rapid, long-distance dispersal by pumice rafting. *PLoS One* 7, e40583. doi:10.1371/journal.pone.0040583
- Bryan, W. B. (1971). Coral sea drift pumice stranded on Eua Island, Tonga, in 1969. *Geol. Soc. Am. Bull.* 82, 2799–2812. doi:10.1130/0016-7606(1971)82[2799:CSDPSO]2.0.CO;2
- Bryant, C. J., Arculus, R. J., and Eggins, S. M. (2003). The geochemical evolution of the Izu-Bonin arc system: A perspective from tephra recovered by deep-sea drilling. *Geochem. Geophys. Geosyst.* 4. doi:10.1029/2002GC000427
- Burgisser, A., and Gardner, J. E. (2004). Experimental constraints on degassing and permeability in volcanic conduit flow. *Bull. Volcanol.* 67, 42–56. doi:10.1007/s00445-004-0359-5
- Büttner, R., Dellino, P., and Zimanowski, B. (1999). Identifying magma-water interaction from the surface features of ash particles. *Nature* 401, 688–690. doi:10.1038/44364
- Büttner, R., Dellino, P., la Volpe, L., Lorenz, V., and Zimanowski, B. (2002). Thermohydraulic explosions in phreatomagmatic eruptions as evidenced by the

Publisher's note

All claims expressed in this article are solely those of the authors and do not necessarily represent those of their affiliated organizations, or those of the publisher, the editors and the reviewers. Any product that may be evaluated in this article, or claim that may be made by its manufacturer, is not guaranteed or endorsed by the publisher.

Supplementary material

The Supplementary Material for this article can be found online at: <https://www.frontiersin.org/articles/10.3389/feart.2022.963392/full#supplementary-material>

- comparison between pyroclasts and products from Molten Fuel Coolant Interaction experiments. *J. Geophys. Res.* 107, ECV 5-1–ECV 5-14. doi:10.1029/2001jb000511
- Candy, I., Tye, G., Coxon, P., Hardiman, M., Matthews, I., and Palmer, A. (2021). A tephra-based correlation of marine and terrestrial records of MIS 11c from Britain and the North Atlantic. *J. Quat. Sci.* 36, 1149–1161. doi:10.1002/jqs.3367
- Carey, R. J., Wysoczanski, R., Wunderman, R., and Jutzeler, M. (2014). Discovery of the largest historic silicic submarine eruption. *Eos Trans. AGU*, 95, 157–159. doi:10.1002/2014EO190001
- Carey, R., Adam Soule, S., Manga, M., White, J. D. L., McPhie, J., Wysoczanski, R., et al. (2018). The largest deep-ocean silicic volcanic eruption of the past century. *Sci. Adv.* 4, e1701121–e1701127. doi:10.1126/sciadv.1701121
- Castro, J. M., Bindeman, I. N., Tuffen, H., and Ian Schipper, C. (2014). Explosive origin of silicic lava: Textural and $\delta D-H$ 2 O evidence for pyroclastic degassing during rhyolite effusion. *Earth Planet. Sci. Lett.* 405, 52–61. doi:10.1016/j.epsl.2014.08.012
- Dellino, P., Gudmundsson, M. T., Larsen, G., Mele, D., Stevenson, J. A., Thordarson, T., et al. (2012). Ash from the Eyjafjallajökull eruption (Iceland): Fragmentation processes and aerodynamic behavior. *J. Geophys. Res.* 117, 1–10. doi:10.1029/2011JB008726
- Denton, J. S., Tuffen, H., Gilbert, J. S., and Odling, N. (2009). The hydration and alteration of perlite and rhyolite. *J. Geol. Soc. Lond.* 166, 895–904. doi:10.1144/0016-76492008-007
- Denton, J. S., Tuffen, H., and Gilbert, J. S. (2012). Variations in hydration within perlitised rhyolitic lavas—evidence from Torfajökull, Iceland. *J. Volcanol. Geotherm. Res.* 223 (224), 64–73. doi:10.1016/j.jvolgeores.2012.02.005
- di Roberto, A., Albert, P. G., Colizza, E., del Carlo, P., di Vincenzo, G., Gallerani, A., et al. (2020). Evidence for a large-magnitude Holocene eruption of mount rittmann (Antarctica): A volcanological reconstruction using the marine tephra record. *Quat. Sci. Rev.* 250, 106629. doi:10.1016/j.quascirev.2020.106629
- Dingwell, D. B., Lavallée, Y., Hess, K. U., Flaws, A., Marti, J., Nichols, A. R. L., et al. (2016). Eruptive shearing of tube pumice: Pure and simple. *Solid earth*, 7, 1383–1393. doi:10.5194/se-7-1383-2016
- Dingwell, D. B., and Webb, S. L. (1989). Structural relaxation in silicate melts and non-Newtonian melt rheology in geologic processes. *Phys. Chem. Min.* 16, 508–516. doi:10.1007/BF00197020
- Dingwell, D. B., and Webb, S. L. (1990). Relaxation in silicate melts. *Eur. J. Mineral.* 2, 427–451. doi:10.1127/ejm/2/4/0427
- Dürrig, T., Gudmundsson, M. T., Karmann, S., Zimanowski, B., Dellino, P., Rietze, M., et al. (2015). Mass eruption rates in pulsating eruptions estimated from video analysis of the gas thrust-buoyancy transition—A case study of the 2010 eruption of eyjafjallajökull, Iceland. *Earth Planets Space* 67, 180. doi:10.1186/s40623-015-0351-7
- Fiske, R. S., Cashman, K. v., Shibata, A., and Watanabe, K. (1998). Tephra dispersal from Myojinsho, Japan, during its shallow submarine eruption of 1952–1953. *Bull. Volcanol.* 59, 262–275. doi:10.1007/s0044500450190

- Fiske, R. S., Naka, J., Iizasa, K., Yuasa, M., and Klaus, A. (2001). Submarine silicic caldera at the front of the Izu-Bonin arc, Japan: Voluminous seafloor eruptions of rhyolite pumice. *Geol. Soc. Am. Bull.* 113, 813–824. doi:10.1130/0016-7606(2001)113<0813:sscatf>2.0.co;2
- Freundt, A., Schindlbeck-Belo, J. C., Kutterolf, S., and Hopkins, J. L. (2021). *Tephra layers in the marine environment: A review of properties and emplacement processes*. London: Geological Society. Special Publications SP520-2021–50. doi:10.1144/sp520-2021-50
- Frick, C., and Kent, L. E. (1984). Drift pumice in the Indian and south atlantic oceans. *South Afr. J. Geol.* 87, 19–33.
- Friedman, I., and Smith, R. L. (1958). The deuterium content of water in some volcanic glasses. *Geochim. Cosmochim. Acta* 15, 218–228. doi:10.1016/0016-7037(58)90059-0
- Fujii, S., and Fuji, N. (1967). Postglacial Sea level in the Japanese islands. *J. Geoscience, Osaka City Univ.* 10, 43–51.
- Fuller, S., Carey, S., and Nomikou, P. (2018). Distribution of fine-grained tephra from the 1650 CE submarine eruption of Kolumbo volcano, Greece. *J. Volcanol. Geotherm. Res.* 352, 10–25. doi:10.1016/j.jvolgeores.2018.01.004
- Gerlach, T. M., Westrich, H. R., and Symonds, R. B. (1996). "Preeruption vapor in magma of the climactic Mount Pinatubo eruption: Source of the giant stratospheric sulfur dioxide cloud," in *FIRE and MUD: Eruptions and lahars of mount Pinatubo* (Philippines).
- Giachetti, T., Gonnermann, H. M., Gardner, J. E., Shea, T., and Gouldstone, A. (2015). Discriminating secondary from magmatic water in rhyolitic matrix-glass of volcanic pyroclasts using thermogravimetric analysis. *Geochim. Cosmochim. Acta* 148, 457–476. doi:10.1016/j.gca.2014.10.017
- Giachetti, T., Hudak, M. R., Shea, T., Bindeman, I. N., and Hoxsie, E. C. (2020). D/H ratios and H₂O contents record degassing and rehydration history of rhyolitic magma and pyroclasts. *Earth Planet. Sci. Lett.* 530, 115909. doi:10.1016/j.epsl.2019.115909
- Giachetti, T., and Gonnermann, H. M. (2013). Water in volcanic pyroclast: Rehydration or incomplete degassing? *Earth Planet. Sci. Lett.* 369–370, 317–332. doi:10.1016/j.epsl.2013.03.041
- Giordano, D., Nichols, A. R. L., and Dingwell, D. B. (2005). Glass transition temperatures of natural hydrous melts: A relationship with shear viscosity and implications for the welding process. *J. Volcanol. Geotherm. Res.* 142, 105–118. doi:10.1016/j.jvolgeores.2004.10.015
- Gonnermann, H. M., and Manga, M. (2007). The fluid mechanics inside a volcano. *Annu. Rev. Fluid Mech.* 39, 321–356. doi:10.1146/annurev.fluid.39.050905.110207
- Gottsmann, J., and Dingwell, D. B. (2001). Cooling dynamics of spatter-fed phonolite obsidian flows on Tenerife, Canary Islands. *J. Volcanol. Geotherm. Res.* 105, 323–342. doi:10.1016/S0377-0273(00)00262-6
- Gottsmann, J., and Dingwell, D. B. (2002). The thermal history of a spatter-fed lava flow: The 8-ka pantellerite flow of Mayor Island, New Zealand. *Bull. Volcanol.* 64, 410–422. doi:10.1007/s00445-002-0220-7
- Graettinger, A. H., Valentine, G. A., Sonder, I., Ross, P. S., White, J. D. L., and Taddeucci, J. (2014). Maar-diatreme geometry and deposits: Subsurface blast experiments with variable explosion depth. *Geochem. Geophys. Geosyst.* 15, 740–764. doi:10.1002/2013gc005198
- Hamuro, K., Aramaki, S., Fujioka, K., Ishii, T., and Tanaka, T. (1983). *Higashi-izu-oki submarine volcanoes, Part 2, and the submarine volcanoes near the Izu shoto islands*. Bulletin of the Earthquake Research Institute, University of Tokyo.
- Helo, C., Longpré, M. A., Shimizu, N., Clague, D. A., and Stix, J. (2011). Explosive eruptions at mid-ocean ridges driven by CO₂-rich magmas. *Nat. Geosci.* 4, 260–263. doi:10.1038/ngeo1104
- Helo, C., Clague, D. A., Dingwell, D. B., and Stix, J. (2013). High and highly variable cooling rates during pyroclastic eruptions on Axial Seamount, Juan de Fuca Ridge. *J. Volcanol. Geotherm. Res.* 253, 54–64. doi:10.1016/j.jvolgeores.2012.12.004
- Hess, K. U., and Dingwell, D. B. (1996). Viscosities of hydrous leucogranitic melts: A non-arrhenian model. *Am. Mineralogist* 81, 1297–1300. doi:10.2138/am-1996-9-1031
- Hudak, M. R., Bindeman, I. N., Loewen, M. W., and Giachetti, T. (2021). Syn-eruptive hydration of volcanic ash records pyroclast-water interaction in explosive eruptions. *Geophys. Res. Lett.* 48, 1–8. doi:10.1029/2021GL094141
- Hudak, M. R., and Bindeman, I. N. (2020). Solubility, diffusivity, and O isotope systematics of H₂O in rhyolitic glass in hydrothermal temperature experiments. *Geochim. Cosmochim. Acta* 283, 222–242. doi:10.1016/j.gca.2020.06.009
- Ikehara, K. (2015). Marine tephra in the Japan Sea sediments as a tool for paleoceanography and paleoclimatology. *Prog. Earth Planet. Sci.* 2, 36. doi:10.1186/s40645-015-0068-z
- Ikehara, K., Usami, K., Kanamatsu, T., Danhara, T., and Yamashita, T. (2017). Three important Holocene tephra off the Pacific coast of the Tohoku region, Northeast Japan: Implications for correlating onshore and offshore event deposits. *Quat. Int.* 456, 138–153. doi:10.1016/j.quaint.2017.08.022
- Ito, K. *Japan meteorological agency report 67. Sumisujima (Smith rocks)*. Available at: https://www.data.jma.go.jp/vois/data/tokyo/STOCK/souran_eng/volcanoes/067_sumisujima.pdf (Accessed December 2022).
- Ito, K. *Japan meteorological agency report 66. Beyonesu (bayonnaise) rocks (including Myojinsho)*. Available at: https://www.data.jma.go.jp/vois/data/tokyo/STOCK/souran_eng/volcanoes/066_beyonesu_rocks.pdf (Accessed December 2022).
- Iwamori, H., Yoshida, K., Nakamura, H., Kuwatani, T., Hamada, M., Haraguchi, S., et al. (2017). Classification of geochemical data based on multivariate statistical analyses: Complementary roles of cluster, principal component, and independent component analyses. *Geochem. Geophys. Geosyst.* 18, 994–1012. doi:10.1002/2016GC006663
- Kano, K. (2003). Subaqueous pumice eruptions and their products: A review. *Geophys. Monogr. Ser.* 140, 213–229. doi:10.1029/140GM14
- Kano, K., Yamamoto, T., and Ono, K. (1996). Subaqueous eruption and emplacement of the shinjima pumice, shinjima (moeshima) island, kagoshima Bay, SW Japan. *J. Volcanol. Geotherm. Res.* 71, 187–206. doi:10.1016/0377-0273(95)00077-1
- Kato, Y. (1987). Woody pumice generated with submarine eruption. *Jour. Geol. Soc. Jpn.* 93, 11–20. doi:10.5575/geosoc.93.11
- Kato, Y. (1988). Gray pumices drifted from fukutoku-oka-no-ba to the ryukyuu islands. *Bull. Volcanol. Soc. Jpn.* 33, 21–30. doi:10.18940/kazanc.33.1_21
- Kazuo Seki (1927). 軽石の漂流に就て. *海洋気象台彙報* 10, 1–42.
- Kienle, J., Kyle, P. R., Self, S., Motyka, R. J., and Lorenz, V. (1980). Ukinrek Maars, Alaska, I. April 1977 eruption sequence, petrology and tectonic setting. *J. Volcanol. Geotherm. Res.* 7, 11–37. doi:10.1016/0377-0273(80)90018-9
- Kimura, J. I., Nagahashi, Y., Satoguchi, Y., and Chang, Q. (2015). Origins of felsic magmas in Japanese subduction zone: Geochemical characterizations of tephra from caldera-forming eruptions <5 Ma. *Geochem. Geophys. Geosyst.* 16, 2147–2174. doi:10.1002/2015GC005854
- Kobayashi, M., Aoki, K., Murata, M., Nishizawa, F., and Suzuki, T. (2020). Tephrostratigraphy and eruption history after Miyatsukayama event on Niijima volcano, Izu islands, Japan. *Bull. Volcanol. Soc. Jpn.* 65, 21–40. doi:10.18940/kazan.65.2_21
- Kutterolf, S., Schindlbeck, J. C., Scudder, R. P., Murray, R. W., Pickering, K. T., Freundt, A., et al. (2014). Large volume submarine ignimbrites in the shikoku basin: An example for explosive volcanism in the western pacific during the late miocene. *Geochem. Geophys. Geosyst.* 15, 1837–1851. doi:10.1002/2014GC005263
- Kutterolf, S., Schindlbeck, J. C., Robertson, A. H. F., Avery, A., Baxter, A. T., Petronotis, K., et al. (2018). Tephrostratigraphy and provenance from IODP expedition 352, Izu-Bonin arc: Tracing tephra sources and volumes from the oligocene to recent. *Geochem. Geophys. Geosyst.* 19, 150–174. doi:10.1002/2017GC007100
- Kutterolf, S., Freundt, A., Druitt, T. H., McPhie, J., Nomikou, P., Pank, K., et al. (2021a). The medial offshore record of explosive volcanism along the central to eastern aegean volcanic arc: 2. Tephra ages and volumes, eruption magnitudes and marine sedimentation rate variations. *Geochem. Geophys. Geosyst.* 22. doi:10.1029/2021GC010011
- Kutterolf, S., Freundt, A., Hansteen, T. H., Dettbarn, R., Hampel, F., Sievers, C., et al. (2021b). The medial offshore record of explosive volcanism along the central to eastern aegean volcanic arc: 1. Tephrostratigraphic correlations. *Geochem. Geophys. Geosyst.* 22. doi:10.1029/2021GC010010
- Lambeck, K., Rouby, H., Purcell, A., Sun, Y., and Sambridge, M. (2014). sea level and global ice volumes from the Last glacial maximum to the Holocene. *Proc. Natl. Acad. Sci. U. S. A.* 111, 15296–15303. doi:10.1073/pnas.1411762111
- Lange, R. A., and Carmichael, I. S. E. (1987). Densities of Na₂O-K₂O-CaO-MgO-FeO-Fe₂O₃-Al₂O₃-TiO₂-SiO₂ liquids: New measurements and derived partial molar properties. *Geochim. Cosmochim. Acta* 51, 2931–2946. doi:10.1016/0016-7037(87)90368-1
- Long, W., and Friedman, I. (1968). The refractive index of experimentally hydrated rhyolite glass. *Am. J. Sci.* 53, 1754–1756.
- Lowe, D. J. (2011). Tephrochronology and its application: A review. *Quat. Geochronol.* 6, 107–153. doi:10.1016/j.quageo.2010.08.003
- Lowenstern, J. B. (2001). Carbon dioxide in magmas and implications for hydrothermal systems. *Min. Depos.* 36, 490–502. doi:10.1007/s001260100185
- Machida, H. (1999). The stratigraphy, chronology and distribution of distal marker-tephras in and around Japan. *Glob. Planet. Change* 21, 71–94. doi:10.1016/S0921-8181(99)00008-9

- Manga, M., Fauria, K. E., Lin, C., Mitchell, S. J., Jones, M., Conway, C. E., et al. (2018). The pumice raft-forming 2012 Havre submarine eruption was effusive. *Earth Planet. Sci. Lett.* 489, 49–58. doi:10.1016/j.epsl.2018.02.025
- Mangan, M., Mastin, L., and Sisson, T. (2004). Gas evolution in eruptive conduits: Combining insights from high temperature and pressure decompression experiments with steady-state flow modeling. *J. Volcanol. Geotherm. Res.* 129, 23–36. doi:10.1016/S0377-0273(03)00230-0
- McIntosh, I. M., Llewellyn, E. W., Humphreys, M. C. S., Nichols, A. R. L., Burgisser, A., Schipper, C. I., et al. (2014). Distribution of dissolved water in magmatic glass records growth and resorption of bubbles. *Earth Planet. Sci. Lett.* 401, 1–11. doi:10.1016/j.epsl.2014.05.037
- McIntosh, I. M., Nichols, A. R. L., Tani, K., and Llewellyn, E. W. (2017). Accounting for the species-dependence of the 3500 cm⁻¹ H₂O infrared molar absorptivity coefficient: Implications for hydrated volcanic glasses. *Am. Mineralogist* 102, 1677–1689. doi:10.2138/am-2017-5952CCBY
- McIntosh, I. M., Tani, K., Nichols, A. R. L., Chang, Q., and Kimura, J.-I. (2022). Past eruptions of a newly discovered active, shallow, silicic submarine volcano near Tokyo Bay, Japan. *Geology* 50, 1111–1115. doi:10.1130/G50148.1
- Mitchell, S. J., McIntosh, I. M., Houghton, B. F., Carey, R. J., and Shea, T. (2018). Dynamics of a powerful deep submarine eruption recorded in H₂O contents and speciation in rhyolitic glass: The 2012 Havre eruption. *Earth Planet. Sci. Lett.* 494, 135–147. doi:10.1016/j.epsl.2018.04.053
- Mitchell, S. J., Hudak, M. R., Bindeman, I. N., Carey, R. J., McIntosh, I. M., Houghton, B. F., et al. (2022). Isotopic signatures of magmatic fluids and seawater within silicic submarine volcanic deposits. *Geochim. Cosmochim. Acta* 326, 214–233. doi:10.1016/j.gca.2022.03.022
- Moitra, P., Sonder, I., and Valentine, G. A. (2018). Effects of size and temperature-dependent thermal conductivity on the cooling of pyroclasts in air. *Geochim. Geophys. Geosyst.* 19, 3623–3636. doi:10.1029/2018GC007510
- Moitra, P., Sonder, I., and Valentine, G. A. (2020). The role of external water on rapid cooling and fragmentation of magma. *Earth Planet. Sci. Lett.* 537, 116194. doi:10.1016/j.epsl.2020.116194
- Morimoto, R., and Ossaka, J. (1955). *The 1952-1953 submarine eruption of the Myojin reef near the bayonnaise rocks*. Tokyo uni: Japan. Bull. Earthq. Res. Inst.
- Murch, A. P. (2018). *Ash generation in the 2012 eruption of Havre volcano, Kermadec arc: The largest deep subaqueous eruption of the Last century*. (Thesis, Doctor of Philosophy). Dunedin, New Zealand: University of Otago.
- Newman, S., and Lowenstern, J. B. (2002). Volatilecalc: A silicate melt-H₂O-CO₂ solution model written in visual basic for excel. *Comput. Geosci.* 28, 597–604. doi:10.1016/S0098-3004(01)00081-4
- Newman, S., Stolper, E. M., and Epstein, S. (1986). Measurement of water in rhyolitic glasses: Calibration of an infrared spectroscopic technique. *Am. Mineralogist* 71, 1527–1541.
- Ni, H., and Zhang, Y. (2008). H₂O diffusion models in rhyolitic melt with new high pressure data. *Chem. Geol.* 250, 68–78. doi:10.1016/j.chemgeo.2008.02.011
- Nichols, A. R. L., and Wysoczanski, R. J. (2007). Using micro-FTIR spectroscopy to measure volatile contents in small and unexposed inclusions hosted in olivine crystals. *Chem. Geol.* 242, 371–384. doi:10.1016/j.chemgeo.2007.04.007
- Nishimura, A., Rodolfo, K. S., Koizumi, A., Gill, J., and Fujioka, K. (1992). Episodic deposition of pliocene-pleistocene pumice from the Izu-Bonin arc, leg 126. *Proc. Ocean Drill. Program. Sci. Results* 126, 3–22. doi:10.2973/odp.proc.sr.126.115.1992
- Nowak, M., and Behrens, H. (2001). Water in rhyolitic magmas: Getting a grip on a slippery problem. *Earth Planet. Sci. Lett.* 184, 515–522. doi:10.1016/S0012-821X(00)00343-5
- Ochs, F. A., III, and Lange, R. A. (1997). The partial molar volume, thermal expansivity, and compressibility of H₂O in NaAlSi₃O₈ liquid: New measurements and an internally consistent model. *Contributions Mineralogy Petrology* 129, 155–165. doi:10.1007/s004100050329
- Oikawa, T. (2021). “Eruption in august 2021 at Fukutoku okanoba, ogasawara islands,” in *Volcanological society of Japan fall meeting 2021*.
- Oikawa, T., and Tani, K. (2020). Eruption ages of the younger stage of Toshima volcano, Izu islands, Japan, based on ¹⁴C dating and topographical analysis. *Bull. Volcanol. Soc. Jpn.* 65, 83–87. doi:10.18940/kazan.65.3_83
- Okumura, S., Nakamura, M., and Nakashima, S. (2003). Determination of molar absorptivity of IR fundamental OH-stretching vibration in rhyolitic glasses. *Am. Mineralogist* 88, 1657–1662. doi:10.2138/am-2003-11-1204
- Okuno, J., Nakada, M., Ishii, M., and Miura, H. (2014). Vertical tectonic crustal movements along the Japanese coastlines inferred from late Quaternary and recent relative sea-level changes. *Quat. Sci. Rev.* 91, 42–61. doi:10.1016/j.quascirev.2014.03.010
- Palladino, D. M., Valentine, G. A., Sottoli, G., and Taddeucci, J. (2015). Maars calderas: End-members on a spectrum of explosive volcanic depressions. *Front. Earth Sci. (Lausanne)* 3, 1–8. doi:10.3389/feart.2015.00036
- Pattan, J. N., Mudholkar, A. v., Jai Sankar, S., and Ilangoan, D. (2008). Drift pumice in the central Indian ocean basin: Geochemical evidence. *Deep Sea Res. Part I Oceanogr. Res. Pap.* 55, 369–378. doi:10.1016/j.dsr.2007.12.005
- Ponomareva, V., Portnyagin, M., and Davies, S. M. (2015). Tephra without borders: Far-reaching clues into past explosive eruptions. *Front. Earth Sci. (Lausanne)* 3, 1–16. doi:10.3389/feart.2015.00083
- Potuzak, M., Nichols, A. R. L., Dingwell, D. B., and Clague, D. A. (2008). Hyperquenched volcanic glass from loihi seamount, Hawaii. *Earth Planet. Sci. Lett.* 270, 54–62. doi:10.1016/j.epsl.2008.03.018
- Proussevitch, A., and Sahagian, D. (2005). Bubbledrive-1: A numerical model of volcanic eruption mechanisms driven by disequilibrium magma degassing. *J. Volcanol. Geotherm. Res.* 143, 89–111. doi:10.1016/j.jvolgeores.2004.09.012
- Rausch, J., and Schmincke, H. U. (2010). Nejapa Tephra: The youngest (c. 1kaBP) highly explosive hydroclastic eruption in Western Managua (Nicaragua). *J. Volcanol. Geotherm. Res.* 192, 159–177. doi:10.1016/j.jvolgeores.2010.02.010
- Reimer, P. J., Baillie, M. G. L., Bard, E., Bayliss, A., Warren Beck, J., Bertrand, C. J. H., et al. (2004). IntCal04 terrestrial radiocarbon age calibration, 0–26 cal kyr BP. *Radiocarbon* 46, 1029–1058. doi:10.1017/S0033822200032999
- Reimer, P. J., Austin, W. E. N., Bard, E., Bayliss, A., Blackwell, P. G., Bronk Ramsey, C., et al. (2020). The IntCal20 northern hemisphere radiocarbon age calibration curve (0–55 cal kyr BP). *Radiocarbon* 62, 725–757. doi:10.1017/RDC.2020.41
- Saito, K., and Miyairi, Y. (2008). “AMS-¹⁴C dating of charcoal and paleosols from Izu-Oshima and Nijijima Islands: Remarks on eruption ages of rhyolite volcanoes in the northern part of Izu Arc,” in *Proceedings of the 10th Japanese symposium on accelerator mass spectrometry* (Tokyo: Accelerator Management Department, Department of Nuclear Energy, Graduate School of Engineering, The University of Tokyo), 214–217.
- Schipper, C. I., Castro, J. M., Tuffen, H., James, M. R., and How, P. (2013). Shallow vent architecture during hybrid explosive-effusive activity at Cordón Caulle (Chile, 2011–12): Evidence from direct observations and pyroclast textures. *J. Volcanol. Geotherm. Res.* 262, 25–37. doi:10.1016/j.jvolgeores.2013.06.005
- Self, S., Kienle, J., and Huot, J. P. (1980). Ukinrek Maars, Alaska, II. Deposits and formation of the 1977 craters. *J. Volcanol. Geotherm. Res.* 7, 39–65. doi:10.1016/0377-0273(80)90019-0
- Seligman, A. N., Bindeman, I. N., Watkins, J. M., and Ross, A. M. (2016). Water in volcanic glass: From volcanic degassing to secondary hydration. *Geochim. Cosmochim. Acta* 191, 216–238. doi:10.1016/j.gca.2016.07.010
- Shiraishi, T., Arai, F., and Fujimoto, Y. (1992). Discovery of aso-4 ash and drift pumice of aso-4 pyroclastic flow and sambe-kisuki pumice fall deposits in the upper quaternary of the oga peninsula, akita prefecture, northeast honshu, Japan. *Daiyonki-kenkyu.* 31, 21–27. doi:10.4116/jaqua.31.21
- Sparks, R. S. J. (1978). The dynamics of bubble formation and growth in magmas: A review and analysis. *J. Volcanol. Geotherm. Res.* 3, 1–37. doi:10.1016/0377-0273(78)90002-1
- Stevenson, R. J., Dingwell, D. B., Webb, S. L., and Bagdassarov, N. S. (1995). The equivalence of enthalpy and shear stress relaxation in rhyolitic obsidians and quantification of the liquid-glass transition in volcanic processes. *J. Volcanol. Geotherm. Res.* 68, 297–306. doi:10.1016/0377-0273(95)00015-1
- Stolper, E. M. (1982a). The speciation of water in silicate melts. *Geochim. Cosmochim. Acta* 46, 2609–2620. doi:10.1016/0016-7037(82)90381-7
- Stolper, E. M. (1982b). Water in silicate glasses: An infrared spectroscopic study. *Contr. Mineral. Pet.* 81, 1–17. doi:10.1007/bf00371154
- Sweeney, M. R., and Valentine, G. A. (2015). Transport and mixing dynamics from explosions in debris-filled volcanic conduits: Numerical results and implications for maar-diatreme volcanoes. *Earth Planet. Sci. Lett.* 425, 64–76. doi:10.1016/j.epsl.2015.05.038
- Takahashi, T., Aoki, K., Murata, M., Kobayashi, M., and Suzuki, T. (2022). Late Pleistocene stratigraphy of rhyolite tephra beds in Toshima, northern Izu Islands. *Daiyonki-kenkyu.* 61, 2104–2107. doi:10.4116/jaqua.61.2104
- Tamura, Y., and Tatsumi, Y. (2002). Remelting of an andesitic crust as a possible origin for rhyolitic magma in oceanic arcs: An example from the Izu-Bonin arc. *J. Petrology* 43, 1029–1047. doi:10.1093/petrology/43.6.1029
- Tani, K., Fiske, R. S., Tamura, Y., Kido, Y., Naka, J., Shukuno, H., et al. (2008). Sumisu volcano, Izu-Bonin arc, Japan: Site of a silicic caldera-forming eruption from a small open-ocean island. *Bull. Volcanol.* 70, 547–562. doi:10.1007/s00445-007-0153-2
- Tani, K., Ishizuka, O., Nichols, A. R., Hirahara, Y., Carey, R., McIntosh, I. M., et al. (2013). *Discovery of an active shallow submarine silicic volcano in the northern Izu*

Bonin arc: Volcanic structure and potential hazards of Oomurodashii volcano. San Francisco: AGU Fall Meeting.

Taylor, B. (1992). Rifting and the volcanic-tectonic evolution of the Izu-Bonin-Mariana arc. *Proc. Ocean Drill. Program, Sci. Results* 126, 627–652. doi:10.2973/odp.proc.sr.126.163.1992

Uesugi, Y., Shinkawa, K., and Kigoshi, K. (1994). Tephra outcropping along the so-called “chisoh-setudanmen” roadcuts, Sembazaki, Izu-Oshima volcano, Central Japan: Standard tephra columns. *Daiyonki-kenkyu.* 33, 165–187. doi:10.4116/jaqua.33.165

Uemitsu, M. (1991). Holocene sea-level changes and coastal evolution in Japan. *Daiyonki-kenkyu.* 30, 187–196. doi:10.4116/jaqua.30.187

Wallace, P. J., Dufek, J., Anderson, A. T., and Zhang, Y. (2003). Cooling rates of Plinian-fall and pyroclastic-flow deposits in the Bishop Tuff: Inferences from water speciation in quartz-hosted glass inclusions. *Bull. Volcanol.* 65, 105–123. doi:10.1007/s00445-002-0247-9

Ward, W. T., and Little, I. P. (2000). Sea-rafted pumice on the Australian East Coast: Numerical classification and stratigraphy. *Aust. J. Earth Sci.* 47, 95–109. doi:10.1046/j.1440-0952.2000.00763.x

White, J. D. L., and Houghton, B. F. (2006). Primary volcanoclastic rocks. *Geol.* 34, 677–680. doi:10.1130/G22346.1

White, J. D. L., and Ross, P. S. (2011). Maar-diatreme volcanoes: A review. *J. Volcanol. Geotherm. Res.* 201, 1–29. doi:10.1016/j.jvolgeores.2011.01.010

Wilding, M., Dingwell, D., Batiza, R., Wilson, L., and Wilding, M. (2000). Cooling rates of hyaloclastites: Applications of relaxation geospeedometry to undersea volcanic deposits. *Bull. Volcanol.* 61, 527–536. doi:10.1007/s004450050003

Wysoczanski, R., and Tani, K. (2006). Spectroscopic FTIR imaging of water species in silicic volcanic glasses and melt inclusions: An example from the Izu-Bonin arc. *J. Volcanol. Geotherm. Res.* 156, 302–314. doi:10.1016/j.jvolgeores.2006.03.024

Xu, Z., and Zhang, Y. (2002). Quench rates in air, water, and liquid nitrogen, and inference of temperature in volcanic eruption columns. *Earth Planet. Sci. Lett.* 200, 315–330. doi:10.1016/S0012-821X(02)00656-8

Yeo, I. A., McIntosh, I. M., Bryan, S. E., Tani, K., Dunbabin, M., Metz, D., et al. (2022). The 2019–2020 volcanic eruption of Late’iki (Metis Shoal), Tonga. *Sci. Rep.* 12, 7468. doi:10.1038/s41598-022-11133-8

Yuasa, M., and Kano, K. (2003). Submarine silicic calderas on the northern Shichito-Iwojima ridge, Izu-Ogasawara (Bonin) arc, Western Pacific. *Geophys. Monogr. Ser.* 140, 231–243. doi:10.1029/140GM15

Yuasa, M., Murakami, F., Saito, E., and Watanabe, K. (1991). Submarine topography of seamounts on the volcanic front of the Izu-Ogasawara (Bonin) Arc. *Bull. Geol. Surv. Jpn.* 42, 703–743.

Zhang, Y., and Behrens, H. (2000). H₂O diffusion in rhyolitic melts and glasses. *Chem. Geol.* 169, 243–262. doi:10.1016/S0009-2541(99)00231-4

Zhang, Y., and Ni, H. (2010). Diffusion of H, C, and O components in silicate melts. *Rev. Mineral. Geochem.* 72, 171–225. doi:10.2138/rmg.2010.72.5

Zhang, Y. (1994). Reaction kinetics, geospeedometry, and relaxation theory. *Earth Planet. Sci. Lett.* 122, 373–391. doi:10.1016/0012-821x(94)90009-4

Zhang, Y. (1999). H₂O in rhyolitic glasses and melts: Measurement, speciation, solubility, and diffusion. *Rev. Geophys.* 37, 493–516. doi:10.1029/1999RG900012

Zhang, Y., Stolper, E. M., and Wasserburg, G. J. (1991). Diffusion of water in rhyolitic glasses. *Geochim. Cosmochim. Acta* 55, 441–456. doi:10.1016/0016-7037(91)90003-N

Zhang, Y., Stolper, E. M., and Ihinger, P. D. (1995). Kinetics of the reaction H₂O + O = 2OH in rhyolitic and albite glasses: Preliminary results. *Am. Mineralogist* 80, 593–612. doi:10.2138/am-1995-5-618

Zhang, Y., Jenkins, J., and Xu, Z. (1997). Kinetics of the reaction H₂O + O → 2OH in rhyolitic glasses upon cooling: Geospeedometry and comparison with glass transition. *Geochim. Cosmochim. Acta* 61, 2167–2173. doi:10.1016/s0016-7037(97)00054-9

Zhang, Y., Xu, Z., and Behrens, H. (2000). Hydrous species geospeedometer in rhyolite: Improved calibration and application. *Geochim. Cosmochim. Acta* 64, 3347–3355. doi:10.1016/S0016-7037(00)00424-5

Zhang, Y., Xu, Z., and Liu, Y. (2003). Viscosity of hydrous rhyolitic melts inferred from kinetic experiments, and a new viscosity model. *Am. Mineralogist* 88, 1741–1752. doi:10.2138/am-2003-11-1215